Dynamic state-space estimation of the hemodynamic response with Near-Infrared Spectroscopy
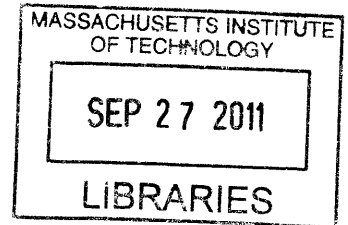
by

Louis Gagnon

B.S. Engineering Physics, M.S. Biomedical Engineering
Ecole Polytechnique de Montreal

Submitted to the Department of Electrical Engineering and Computer Science
in partial fulfillment of the requirements for the degree of

Master of Science in Electrical Engineering and Computer Science

at the

MASSACHUSETTS INSTITUTE OF TECHNOLOGY

September 2011

Author . . . .
Department of Electrical Engineering and Computer Science
September 7, 2011

Certified by . . . .
David A. Boas
Associate Professor of Radiology
Thesis Supervisor

Accepted by . . . .
Leslie A. Kolodziejski
Chair, Department Committee on Graduate Students

Dynamic state-space estimation of the hemodynamic response with Near-Infrared Spectroscopy

by

Louis Gagnon

B.S. Engineering Physics, M.S. Biomedical Engineering

Ecole Polytechnique de Montreal

Abstract

Near-Infrared Spectroscopy (NIRS) allows the recovery of the hemodynamic response associated with evoked brain activity. The signal is contaminated with systemic physiological interference which occurs in the superficial layers of the head as well as in the brain tissue. The back-reflection geometry of the measurement makes the DOI signal strongly contaminated by systemic interference occurring in the superficial layers. A recent development has been the use of signals from small source-detector separation (1 cm) optodes as regressors. Since those additional measurements are mainly sensitive to superficial layers in adult humans, they help in removing the systemic interference present in longer separation measurements (3 cm). Encouraged by those findings, we developed a dynamic estimation procedure to remove global interference using small optode separations and to estimate simultaneously the hemodynamic response. The algorithm was tested by recovering a simulated synthetic hemodynamic response added over baseline DOI data acquired from 6 human subjects at rest. The performance of the algorithm was quantified by the Pearson R^2 coefficient and the mean square error (MSE) between the recovered and the simulated hemodynamic responses. Our dynamic estimator was also compared with a static estimator and the traditional adaptive filtering method. We observed a significant improvement (two-tailed paired t-test, $p < 0.05$) in both HbO and HbR recovery using our Kalman filter dynamic estimator compared to the traditional adaptive filter, the static estimator and the standard GLM technique. We then show that the systemic interference occurring in the superficial layers of the human head is inhomogeneous across the surface of the scalp. As a result, the improvement obtained by using a short separation optode decreases as the relative distance between the short and the long measurement

is increased. NIRS data was acquired on 6 human subjects both at rest and during a motor task consisting of finger tapping. The effect of distance between the short and the long channel was first quantified by recovering a synthetic hemodynamic response added over the resting-state data. The effect was also observed in the functional data collected during the finger tapping task. Together, these results suggest that the short separation measurement must be located as close as 1.5 cm from the standard NIRS channel in order to provide an improvement which is of practical use. In this case, the improvement in Contrast-to-Noise Ratio (CNR) compared to a standard GLM procedure without using any small separation optode reached 50% for HbO and 100% for HbR. Using small separations located farther than 2 cm away resulted in mild or negligible improvements only.

Thesis Supervisor: David A. Boas
Title: Associate Professor of Radiology

Acknowledgments

Contents

List of Figures

List of Tables

Chapter 1

Introduction

Diffuse optical imaging (DOI) is an experimental technique that uses near-infrared spectroscopy (NIRS) to image biological tissue [48, 37, 13, 19, 20]. The dominant chromophores in this spectrum are the two forms of hemoglobin: oxygenated hemoglobin (HbO) and reduced hemoglobin (HbR). In the past 15 years, this technique has been used for the noninvasive measurement of the hemodynamic changes associated with evoked brain activity [48, 20].

Compared with other existing functional imaging methods e.g., functional Magnetic Resonance Imaging (fMRI), Positron Emission Tomography (PET), Electroencephalography (EEG), and Magnetoencephalography (MEG), the advantages of DOI for studying brain function include good temporal resolution of the hemodynamic response, measurement of both HbO and HbR, nonionizing radiation, portability, and low cost. Disadvantages include modest spatial resolution and limited penetration depth.

The sensitivity of NIRS to evoked brain activity is also reduced by systemic physiological interference arising from cardiac activity, respiration, and other homeostatic processes [36, 46, 38, 8]. These sources of interference are called global interference or systemic interference. Part of the interference occurs both in the superficial layers of

the head (scalp and skull) and in the brain tissue itself. However, the back-reflection geometry of the measurement makes NIRS significantly more sensitive to the superficial layers as illustrated in Fig. 1-1. As such, the NIRS signal is often dominated by systemic interference occurring in the skin and the skull.
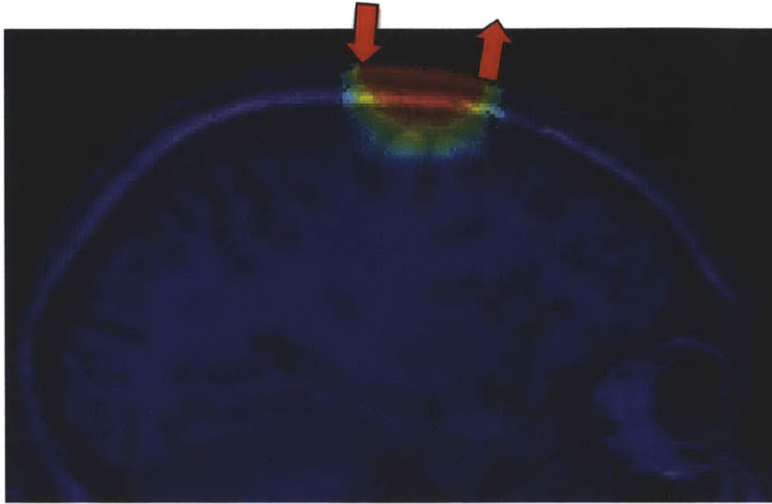
Figure 1-1: Sensitivity profile of a given source-detector pair in NIRS.

Different methods have been used in the literature to remove the systemic interference from DOI measurements. Low pass filtering is widely used in the literature, as it is highly effective at removing cardiac oscillations [9, 29]. However, there is a significant overlap between the frequency spectrum of the hemodynamic response to brain activity and the spectrum of other physiological variations such as respiration, spontaneous low frequency oscillations and very low frequency oscillations. Frequency-based removal of these sources of interference can therefore result in large distortion and inaccurate timing for the recovered brain activity signal. As such, more powerful methods for global noise reduction have been developed. These include adaptive average waveform subtraction [15], subtraction of another NIRS source-detector (SD) channel performed over a non-activated region of the brain [9], principal component analysis [50, 10] and finally wavelet filtering [33, 35, 28, 34].

A recent development for removing global interference from NIRS measurements is to use additional optodes in the activated region with small SD separations that are

12

sensitive to superficial layers only [42, 52, 53, 51, 47, 49, 16]. This method is illustrated in Fig. 1-2. Making the assumption that the signal collected in the superficial layers is
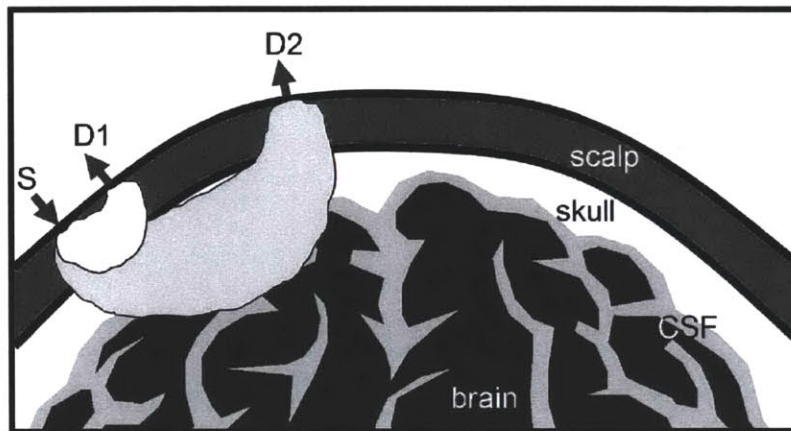
Figure 1-2: Illustration of the short separation regression method in NIRS. (Figure taken from Zhang *et al* [52].)

dominated by systemic physiology which is also dominant in the longer SD separation NIRS channel, those additional measurements can be used as regressors to filter systemic interference from the longer SD separations. Saager et al [41] used additional optodes and a linear minimum mean square estimator (LMMSE) to partially remove the systemic interference in the signal. In a second step, the evoked hemodynamic response was estimated using a traditional block-average method over the different trials. The algorithm was further refined by Zhang et al [52, 53, 51] to consider the non-stationary behavior of the systemic interference. They used an adaptive filtering technique together with additional small separation measurements to filter the systemic interference from the raw signal and then performed the block-average technique to estimate the hemodynamic response in a second step.

Although these methods greatly reduced global interference in NIRS data, the filtering of the systemic interference and the estimation of the hemodynamic response were performed in two steps, which might not be optimal. Previous studies have shown that the simultaneous estimation of the hemodynamic response and removal of the systemic interference using temporal basis functions [32, 39] or auxiliary systemic measurements [7] was possible using state-space modeling. Moreover, Diamond et

al proposed a way to quantify the accuracy of such filtering methods. Real NIRS data collected over the head of human subjects at rest were used to generate realistic noise. A synthetic hemodynamic response was added over the real NIRS baseline time course and the response was then recovered from this noisy data set. The recovered response was then compared with the synthetic one used to generate the time course. This method for evaluating reconstruction algorithms has been reproduced by other groups [33, 35, 34].

The main **objectives** of this work were:

1. To integrate the short separation regression method in a state-space framework.

2. To test the accuracy of the short separation regression for different short optode placements.

The work presented in this thesis gave rise to the following publications and posters:

Gagnon, L., Perdue, K., Greve, D.N., Goldenholz, D., Kaskhedikar, G. and Boas, D.A. (2011). "Improved recovery of the hemodynamic response in diffuse optical imaging using short optode separations and state-space modeling." *NeuroImage* 56(3): 1362-1371.

Gagnon, L., Cooper, R. J., Yucel, M. A., Perdue, K., Greve, D. N. and Boas, D. A. (2011). "Short separation channel location impacts the performance of short channel regression in NIRS." *submitted*

Gagnon, L., Cooper, R. J., Yucel, M. A., Perdue, K. L., Greve, D. N. and Boas, D. A. (2011). "Kalman filter estimator for multi-distance Diffuse Optical Imaging", poster at the *Organization for Human Brain Mapping*, Quebec city, Canada

Gagnon, L., Cooper, R. J., Yucel, M. A., Perdue, K. L., Greve, D. N. and Boas, D. A. (2011). "Dynamic state-space estimation of the hemodynamic response with multi-distance Near-Infrared Spectroscopy", poster at the *24th Annual HST Forum*, Boston, USA

Gagnon, L., Greve,D. N., Perdue, K. L., Goldenholz, D., Kaskhedikar, G., and Boas, D. A. (2010). "Improved recovery of the hemodynamic response using multi-distance NIRS measurements and Kalman filtering techniques", poster at the *Functional Near Infrared Spectroscopy Conference*, Cambridge, USA

Gagnon, L., Mesquita, R. and Boas, D. A. (2009). "Performance of adaptive filtering to remove global interference for the biomechanical modeling of the neurovascular coupling in NIRS", poster at the *SPIE NIH Inter-Institute Workshop on Optical Diagnostic and Biophotonic Methods from Bench to Bedside*, Washington DC, USA

Chapter 2

State-space modeling for NIRS

In the present study, we combined small separation measurements and state-space modeling for the estimation of the hemodynamic response and simultaneous global interference cancellation. We developed both a static and a dynamic estimator. We evaluated the performance of our algorithms using baseline data taken from 6 human subjects at rest and by adding a synthetic hemodynamic response over the baseline measurements. We finally compared our new methods with the adaptive filter [52] and the standard method using no small SD separation measurement.

2.1 Methods

2.1.1 Experimental data

For this study, 6 healthy adult subjects were recruited. The Massachusetts General Hospital Institutional Review Board approved the study and all subjects gave written informed consent. Subjects were instructed to rest while simultaneous BOLD-fMRI and NIRS data were collected. Three 6-minute long runs were collected for each subject. Only the NIRS data was used in this study. The localization and the geometry of the NIRS probe used are shown in Fig. 3-1 a) and b) respectively. Only the two 1 cm SD separation channels and the 8 closest neighbor (3 cm SD separation) channels were used in the analysis.
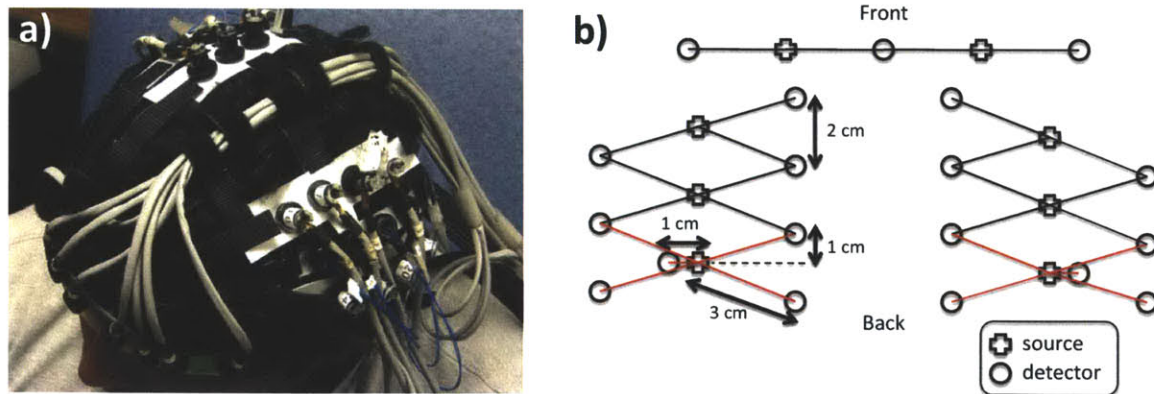
Figure 2-1: a) Position of the probe over the head of the subjects b) Geometry of the optical probe. Two different SD separations were used: 1 cm and 3 cm. The NIRS channels used for the analysis are shown in red.

Changes in optical density for each SD pair were converted to changes in hemoglobin concentrations using the Beer-Lambert relationship [4, 6, 2] and the SD distances illustrated in Fig. 3-1 b). A pathlength correction factor of 6 and a partial volume correction factor of 50 were used for all SD pairs [26, 27].

2.1.2 Synthetic hemodynamic response

To compare the performance of our two algorithms with existing algorithms, a synthetic hemodynamic response was generated using a modified version of a three compartment biomechanical model [25, 23, 22]. Each parameter of the model was set to the middle of its physiological range [25] which results in an HbO increase of 15 μM and an HbR decrease of 7 μM. The amplitude of this synthetic response was of the same order as real motor responses on humans using NIRS and those specific pathlength and partial volume correction factors [27]. These synthetic HbO and HbR responses were then added to the unfiltered concentration data with an inter-stimulus interval taken randomly from a uniform distribution (10-35 s) for each individual trial. Over the six-minute data series, we added either 10, 30 or 60 individual evoked responses. The resulting HbO and HbR time courses were then highpass filtered at 0.01 Hz to remove any drifts and lowpass filtered at 1.25 Hz to remove the instrument noise. The filter used was a 3rd order Butterworth-type filter.

Four different methods were then used to recover the simulated hemodynamic response added to our baseline data. The first two were taken directly from literature and consisted of the standard General Linear Model (GLM) without using a small SD separation measurement and the adaptive filtering (AF) method developed by Zhang et al [52]. The third one was a simultaneous static deconvolution and regression and will be called the static estimator (SE) here for simplicity. The last one was a dynamic Kalman filter estimator (KF).

2.1.3 Signal modeling

For all the methods used in this study, the discrete-time hemodynamic response h at sample time n was reconstructed with a set of temporal basis functions

$$h\left[n\right] = \sum_{i=1}^{N_w} w_i b_i\left[n\right] \tag{2.1}$$

where $b_i[n]$ are normalized Gaussian functions with a standard deviation of 0.5 s and their means separated by 0.5 s over the regression time as shown in Fig. 2-2 a). N_w is the number of Gaussian functions used to model the hemodynamic response and was set to 15 in our work. Using this set, the noise-free simulated HbO response was fit with a Pearson R^2 of 1.00 and a mean square error (MSE) of 9.2×10^{-5} and the noise-free simulated HbR response was fit with an R^2 of 1.00 and an MSE of 2.1×10^{-5}. The MSE was lower for HbR only because the amplitude of the simulated HbR response was lower. These fits are shown in Fig. 2-2 b). The weights for the temporal bases w_i were estimated using the four different methods described in the following sections.
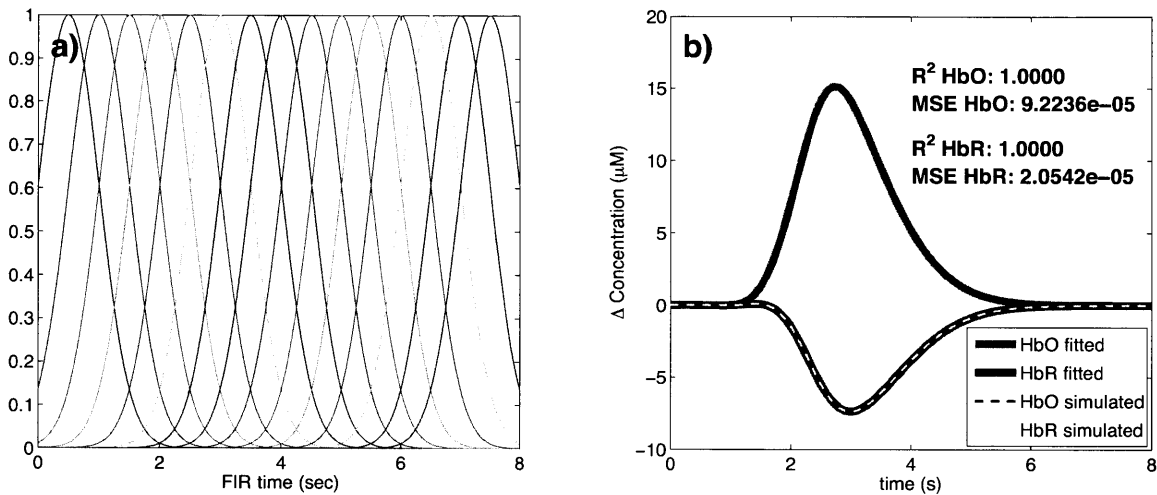
Figure 2-2: a) Temporal basis set used in the analysis. The finite impulse response (FIR) of the temporal basis functions ranged from 0 to 8 s after the onset of the simulated response. b) Noise-free simulated responses (dotted lines) overlapped with the responses recovered with a least-square fit (continuous lines) using the temporal basis set. The R^2 and the MSE of the fit are indicated for both HbO and HbR.

For the standard block average estimator, we modeled the concentration signal in the 3 cm separation channel $y_3[n]$ by

$$y_3[n] = \sum_{k=-\infty}^{\infty} h[k] u[n-k]. \tag{2.2}$$

$u[n]$ is called the onset vector and is a binary vector taking the value 1 when n corresponds to a time where the stimulation starts and 0 otherwise.

19

For our static simultaneous estimator and our dynamic Kalman filter simultaneous estimator, we modeled the signal in the 3 cm separation channel $y_3[n]$ by a linear combination of the 1 cm separation signal $y_1[n]$ and the hemodynamic response $h[n]$ by

$$y_3[n] = \sum_{k=-\infty}^{\infty} h[k]u[n-k] + \sum_{i=1}^{N_a} a_i y_1[n+1-i]. \tag{2.3}$$

N_a is the number of time points taken from the 1 cm separation channel to model the superficial signal in the 3 cm separation channel. This value was set to 1 in our work for all three estimators using short SD separation measurements but could be any integer in principle. The a_i's are the weights used to model the superficial signal in the 3 cm separation channel from the linear combination of the 1 cm separation signal. The states to be estimated by the static and the Kalman filter estimators were the weights for the superficial contribution a_i and the weights for the temporal bases w_i. All those weights were assumed stationary in the case of the static estimator, and time-varying in the case of the Kalman filter estimator.

The motivation for Eq. 3.2 is that the residual between the 3 cm channel and the 1 cm channel corresponds to the hemodynamic response of the brain. This is well justified when the brain activation is detected only in the 3 cm separation channel and when the systemic physiology pollutes both the 1 cm and the 3 cm separation channels. It is a reasonable assumption for cognitive NIRS measurements performed on an adult head. In this case, the hemodynamic response is expected to occur only in the brain tissue and the 1 cm separation channel does not reach the cerebral cortex, making the 1 cm measurement sensitive to scalp and skull fluctuations only. This would also be justified for cognitive measurements on babies by reducing the separation of the 1 cm signal to ensure that this channel remains insensitive to brain hemodynamics. However, our assumption would be violated for specific stimuli (e.g. the Valsalva maneuver) for which the hemodynamic response occurs more globally across the head. Other scenarios that could be troublesome would be if the systemic physiology occurs only in the brain tissue (e.g. an activation-like oscillation a few seconds after the true stimulus response) or if the interference is phase-locked with

the stimulus. In this case, the systemic physiology could potentially be modeled by our temporal basis set (overfitting).

2.1.4 Standard General Linear Model

For this first method, and only for this one, the 1 cm SD separation channels were not used. The pre-filtered concentrations from the 3 cm SD separation were further lowpass filtered at 0.5 Hz using a 3rd order Butterworth filter. Re-expressing Eq. 2.2 in matrix form, we get

$$\mathbf{y}_3 = \mathbf{U}\mathbf{w} \tag{2.4}$$

where $\mathbf{y}_3$ is simply the length N_t time course vector $y_3\,[n]$

$$\mathbf{y}_3 = \left[\begin{array}{ccc} y_3\,[1] & \ldots & y_3\,[N_t] \end{array}\right]^T. \tag{2.5}$$

The columns of $\mathbf{U}$ are the linear convolution of the onset vector $u\,[n]$ with each temporal basis function $b_i\,[n]$

$$\mathbf{U} = \left[\begin{array}{ccc} u * b_1\,[n] & \cdots & u * b_{N_w}\,[n] \end{array}\right] \tag{2.6}$$

and $\mathbf{w}$ is the vector containing the weights for the temporal basis w_i

$$\mathbf{w} = \left[\begin{array}{ccc} w_1 & \ldots & w_{N_w} \end{array}\right]^T. \tag{2.7}$$

The estimates of the weights $\hat{\mathbf{w}}$ are found by inverting Eq. 2.4 using the Moore-Penrose pseudoinverse

$$\hat{\mathbf{w}} = \left(\mathbf{U}^T\mathbf{U}\right)^{-1}\mathbf{U}^T\mathbf{y}_3 \tag{2.8}$$

and the hemodynamic response is finally reconstructed with the estimates of the temporal basis weights $\hat{w}_i$ obtained from $\hat{\mathbf{w}}$.

When the GLM was used without any other estimator (i.e. not as the last step of

the adaptive filter or the Kalman filter), we included a 3rd order polynomial drift as a regressor. This procedure is used regularly in fMRI analysis. In this case, the matrix $\mathbf{U}$ is expanded

$$\mathbf{G} = \begin{bmatrix} \mathbf{U} & \mathbf{D} \end{bmatrix} \tag{2.9}$$

where $\mathbf{D}$ is an N_t by 4 drift matrix given in the 2.5. The estimates of the weights $\hat{\mathbf{w}}$ are found by inverting

$$\hat{\mathbf{w}} = \left(\mathbf{G}^T \mathbf{G}\right)^{-1} \mathbf{G}^T \mathbf{y}_3. \tag{2.10}$$

2.1.5 Adaptive filtering

The adaptive filtering technique was taken directly from [52]. Only the salient points are outlined here. The HbO and the HbR responses were recovered independently and the adaptive filter was used for both. The two pre-filtered concentration signals at 1 cm (y_1) and 3 cm (y_3) were first normalized with respect to their respective standard deviation. This was to ensure that the standard deviation of the two signals used in the computation were close 1 to accelerate the convergence of the algorithm [52]. The output of the filter, $e\,[n]$, is then given by

$$e\,[n] = y_3\,[n] - \sum_{k=0}^{N_a} w_{k,n}\, y_1\,[n-k] \tag{2.11}$$

where the coefficient of the filter, $w_{k,n}$, is updated via the Widrow-Hoff least mean square algorithm [17]:

$$w_{k,n} = w_{k,n-1} + 2\mu e\,[n-1]\, y_1\,[n-k]. \tag{2.12}$$

In our study, w was initialized at $w_{k,1} = \begin{bmatrix} 1 & 0 & 0 & \ldots \end{bmatrix}^T$ and μ was set to $1\mathrm{x}10^{-4}$ as in [52]. After trying different values for N_a, we identified $N_a = 1$ as the value minimizing the MSE between our simulated and recovered hemodynamic responses. The output $e\,[n]$ was then multiplied by the original standard deviation of y_3 to rescale it back to its

original scale. The output of the filter was then further lowpass filtered at 0.5 Hz and the hemodynamic response was finally estimated using the standard GLM method (with no drift) by substituting $\mathbf{y_3}$ by $\mathbf{e}$ in Eq. 2.8

$$\hat{\mathbf{w}} = \left(\mathbf{U}^T\mathbf{U}\right)^{-1}\mathbf{U}^T\mathbf{e} \tag{2.13}$$

where $\mathbf{e}$ is simply the length N_t time course vector $e\left[n\right]$

$$\mathbf{e} = \left[\begin{array}{ccc} e\left[1\right] & \ldots & e\left[N_t\right] \end{array}\right]^T \tag{2.14}$$

and again the hemodynamic response is finally reconstructed with the estimates of the temporal basis weights $\hat{w}_i$ obtained from $\hat{\mathbf{w}}$.

2.1.6   Static estimator

Our static estimator is an improved version of the linear minimum mean square estimator (LMMSE) developed by Saager et al [41, 42]. In their work, they used the small separation signal and an LMMSE to estimate the contribution of the superficial signal in the large separation signal. This superficial contamination was then removed from the large separation signal and the hemodynamic response was then estimated from the residual (large separation signal without the superficial contamination). In our study, we simultaneously removed the contribution of the superficial signal in the 3 cm separation signal and estimated the hemodynamic response.

Eqs. 3.2 and 3.1 can be re-expressed in matrix form

$$\mathbf{y_3} = \mathbf{Ax} \tag{2.15}$$

where $\mathbf{y_3}$ is the vector representing the signal in the 3 cm channel and is given by Eq.

2.5, $\mathbf{x}$ is the concatenation of the w_i's and a_i's

$$\mathbf{x} = \begin{bmatrix} w_1 & \ldots & w_{N_w} & a_1 & \ldots & a_{N_a} \end{bmatrix}^T \tag{2.16}$$

and $\mathbf{A}$ is the concatenation of the N_t by N_w matrix $\mathbf{U}$ given by Eq. 3.6 and the N_t by N_a matrix $\mathbf{Y}$

$$\mathbf{A} = \begin{bmatrix} \mathbf{U} & \mathbf{Y} \end{bmatrix} \tag{2.17}$$

where

$$\mathbf{Y} = \begin{bmatrix} y_1[1] & 0 & \ldots \\ y_1[2] & y_1[1] & 0 \\ \vdots & \vdots & \ddots \end{bmatrix} \tag{2.18}$$

The first N_w columns of $\mathbf{A}$ are the linear convolution of the onset vector $u[n]$ with each temporal basis function $b_i[n]$ and the last N_a columns of $\mathbf{A}$ are simply the signal from the 1 cm separation channel $y_1[n]$ delayed by one more sample in each column. In order to compare the different estimators on the same footing, N_a was set to 1 for all three estimators using short SD separations. A more explicit expression for $\mathbf{A}$ is given in 2.5. The estimates of the weights $\hat{\mathbf{x}}$ are found by inverting Eq. 2.15 using the Moore-Penrose pseudoinverse

$$\hat{\mathbf{x}} = \left(\mathbf{A}^T \mathbf{A} \right)^{-1} \mathbf{A}^T \mathbf{y}_3 \tag{2.19}$$

and the hemodynamic response is finally reconstructed with the estimates of the temporal basis weights $\hat{w}_i$ obtained from $\hat{\mathbf{x}}$. This reconstructed response was further lowpass filtered at 0.5 Hz.

2.1.7 Kalman filter estimator

For our dynamic Kalman filter estimator, Eqs. 3.2 and 3.1 need to be re-express in state-space form:

$$\mathbf{x}[n+1] = \mathbf{I}\mathbf{x}[n] + \mathbf{w}[n] \tag{2.20}$$

24

$$y_3[n] = \mathbf{C}[n]\mathbf{x}[n] + \mathbf{v}[n] \tag{2.21}$$

where $\mathbf{w}[n]$ and $\mathbf{v}[n]$ are the process and the measurement noise respectively. $\mathbf{x}[n]$ is the sample n of $\mathbf{x}$ given by Eq. 3.5, $\mathbf{I}$ is an $N_w + N_a$ by $N_w + N_a$ identity matrix and $\mathbf{C}[n]$ is an $N_w + N_a$ by 1 vector whose entries correspond to the nth row of $\mathbf{A}$ in Eq. 2.17. The estimate $\hat{\mathbf{x}}[n]$ at each sample n is then computed using the Kalman filter [31] followed by the Rauch–Tung–Striebel smoother [40]. The Kalman filter recursions require initialization of the state vector estimate $\hat{\mathbf{x}}[0]$ and estimated state covariance $\mathbf{P}[0]$. In our study, the initial state vector estimate $\hat{\mathbf{x}}[0]$ was set to the values obtained using our static estimator and the initial state covariance estimate $\mathbf{P}[0]$ was set to an identity matrix with diagonal entries of $1\text{x}10^{-1}$ for the temporal basis states and $5\text{x}10^{-4}$ for the superficial contribution state. The Kalman filter algorithm was run a first time to estimate the initial state covariance and then run a second time. The initial covariance estimate for the second run was set to the final covariance estimate of the first run. Running the filter twice makes the method less sensitive to the initial guess $\mathbf{P}[0]$. Statistical covariance priors must also be specified for the state process noise $\text{cov}(\mathbf{w}) = \mathbf{Q}$ and the measurement noise $\text{cov}(\mathbf{v}) = \mathbf{R}$. The process noise determines how big the states are allowed to vary at each time step. If this value is small, the estimator will approach the static estimator. If it is large, the state will be allowed to vary significantly over time. In this work, the process noise covariance only contained nonzero terms on the diagonal elements. Those diagonal terms were set to $2.5\text{x}10^{-6}$ for the temporal basis state and $5\text{x}10^{-6}$ for the superficial contribution states. This imbalance in state update noise was also used by Diamond et al [7] and caused the functional response model to evolve more slowly than the superficial contribution model. Practically, the measurement noise determine how well we trust the measurements during the recovery procedure. In our study, the measurement noise covariance was set to an identity matrix scaled by $5\text{x}10^{-2}$. Different values have been tried for the process noise and the measurement noise covariances. Changing the value of $\mathbf{Q}$ and $\mathbf{R}$ over two orders of magnitude did not result in notable performance changes and we could have drawn all the same

conclusions presented in this paper using these alternative $\mathbf{Q}$ and $\mathbf{R}$ values. The values for $\mathbf{Q}$ and $\mathbf{R}$ presented above were empirically determined to minimize the MSE between the recovered and the simulated hemodynamic response. The algorithm was then processed with the following prediction-correction recursion [12].

Since the state update matrix is the identity matrix in Eq. 3.3, the state vector $\mathbf{x}$ and state covariance $\mathbf{P}$ are predicted with

$$\hat{\mathbf{x}}\left[n|n-1\right] = \hat{\mathbf{x}}\left[n-1|n-1\right] \tag{2.22}$$

$$\hat{\mathbf{P}}\left[n|n-1\right] = \hat{\mathbf{P}}\left[n-1|n-1\right] + \mathbf{Q}. \tag{2.23}$$

The Kalman gain $\mathbf{K}$ is then computed

$$\mathbf{K}\left[n\right] = \hat{\mathbf{P}}\left[n|n-1\right]\mathbf{C}\left[n\right]^{T}\left(\mathbf{C}\left[n\right]\hat{\mathbf{P}}\left[n|n-1\right]\mathbf{C}\left[n\right]^{T} + \mathbf{R}\right)^{-1} \tag{2.24}$$

and the state vector $\mathbf{x}$ and state covariance $\mathbf{P}$ predictions are corrected with the most recent measurements $y_3\left[n\right]$

$$\hat{\mathbf{x}}\left[n|n\right] = \hat{\mathbf{x}}\left[n|n-1\right] + \mathbf{K}_n\left(y_3\left[n\right] - \mathbf{C}\left[n\right]\hat{\mathbf{x}}\left[n|n-1\right]\right) \tag{2.25}$$

$$\hat{\mathbf{P}}\left[n|n\right] = \left(\mathbf{I} - \mathbf{K}\left[n\right]\mathbf{C}\left[n\right]\right)\hat{\mathbf{P}}\left[n|n-1\right]. \tag{2.26}$$

After the Kalman algorithm was applied twice, the Rauch–Tung–Striebel smoother was applied in the backward direction. With the identity matrix as the state-update matrix in Eq. 3.3, the algorithm is given by [18]:

$$\hat{\mathbf{x}}\left[n|N_t\right] = \hat{\mathbf{x}}\left[n|n\right] + \hat{\mathbf{P}}\left[n|n\right]\hat{\mathbf{P}}\left[n+1|n\right]^{-1}\left(\hat{\mathbf{x}}\left[n+1|N_t\right] - \hat{\mathbf{x}}\left[n+1|n\right]\right). \tag{2.27}$$

The complete time course of the estimated hemodynamic response $\hat{h}\left[n\right]$ was then reconstructed for each sample time n using the final state estimates $\hat{\mathbf{x}}\left[n|N_t\right]$ and the

temporal basis set contained in $\mathbf{C}\,[n]$

$$\hat{h}\,[n] = \mathbf{C}\,[n]\,\hat{\mathbf{x}}\,[n|N_t]\,. \tag{2.28}$$

This reconstructed hemodynamic response time course $\hat{h}\,[n]$ was further lowpass filtered at 0.5 Hz and the standard GLM estimator (with no polynomial drift) was then applied

$$\hat{\mathbf{w}} = \left(\mathbf{U}^T\mathbf{U}\right)^{-1}\mathbf{U}^T\hat{\mathbf{h}} \tag{2.29}$$

where $\mathbf{U}$ is the matrix defined in Eq. 3.6 and

$$\hat{\mathbf{h}} = \left[\begin{array}{ccc} \hat{h}\,[1] & \ldots & \hat{h}\,[N_t] \end{array}\right]^T \tag{2.30}$$

to obtain the final weights $\hat{w}_i$ used to reconstructed the final estimate of the hemodynamic response. We observed that these last filtering and averaging steps further improved the estimate of the hemodynamic response compared to reconstructing the hemodynamic response from the final state estimates of the smoother.

2.1.8 Statistical analysis

Only specific channels based on the following criteria were kept in the analysis. The raw hemoglobin concentrations were bandpass filtered with a 3rd order Butterworth-type filter between 0.01 Hz and 1.25 Hz [53]. The Pearson correlation coefficient R^2 between each 1 cm HbO channel and its 4 closest neighbor 3 cm HbO channels (before adding the synthetic hemodynamic response) were then computed and the SD pairs for which $R^2 < 0.1$ were discarded for the analysis. The mean R^2 across the selected channels was 0.47 for HbO and 0.22 for HbR. We also computed the Pearson correlation coefficient after adding the synthetic hemodynamic response and similar results were obtained. The mean differences between the R^2's computed before and after adding the synthetic response was 0.01 for HbO and 0.003 for HbR, with the highest value obtained before adding the synthetic response to the real data.

Those small differences emphasize the fact that the signals were dominated by systemic physiology in our simulations. This result also suggests that no resting state measurement is required to select the channels which would benefit from the small separation measurement since the correlation can be estimated from the time course containing brain activation. Zhang et al [51] showed that the adaptive filter method was working well when the correlation between the short and the long separation channel for HbO was greater than 0.6. We used 0.1 in this work to include more channels in the analysis and to show that our state-space method was working well when the initial correlation was lower than 0.5. Using this criterion, 94 out of the 144 possible channels (6 subjects $\times$ 3 runs $\times$ 8 channels) were kept for further analysis. This represented 65 % of the original data set. The numbers of channels kept for each of the subjects were 16, 14, 13, 17, 19 and 15 respectively. The signal to noise ratio (SNR) for each channel was computed as the amplitude of the simulated hemodynamic response divided by the standard deviation of the time course of the signal. The mean SNR across the selected channels was 0.45 for HbO and 0.38 for HbR.

We used two different metrics to compare the performance of the different algorithms. The first one was the Pearson correlation coefficient R^2 between the true synthetic hemodynamic response and the recovered response given by each algorithm. This metric was used to access the level of oscillation in the recovered hemodynamic response created by the global interference not removed by the algorithms and still contaminating the signal. Since the R^2 coefficient is scale invariant, it could not give any information about the accuracy of the amplitude of the recovered hemodynamic response. To overcome this problem, we also used the mean square error (MSE) as a metric to compare the performance of the different algorithms.

Since the random position of the trials across the same time course can greatly affect the accuracy of the recovered hemodynamic response, we repeated the procedure 30 times with 30 different random onset time instances for each of the 94 selected channels. The mean and the standard deviation of the 2820 R^2 coefficients (94 channels

× 30 instances) for each algorithm were then computed after applying the Fisher transformation

$$z = \tanh^{-1}\left(R^2\right) \tag{2.31}$$

and the results were then inverse transformed. The mean and the standard deviation of the 2820 MSEs were also computed. This procedure was repeated independently for 10, 30 and 60 trials in each six-minute data series. The different algorithms were compared together by computing two-tailed paired t-tests on their MSEs and Fisher transformed R^2 coefficients.

2.2 Results

Typical time courses of the recovered hemodynamic response overlapped with the true simulated response are shown in Fig. 2-3 a) to d) for the four algorithms tested. The SNR for this particular simulation was 0.33 for HbO and 0.81 for HbR. The R^2's and the MSEs for HbO and HbR are shown in the legend of each individual panel. Those individual results were obtained from a single simulation with 10 trials. The time courses for this specific simulation are shown in panel e) for HbO and f) for HbR. Both the initial 1 cm channel and the 3 cm channel containing the added synthetic hemodynamic responses are shown as well as the position of the 10 individual onset times. The R^2 between the initial 1 cm channel and the initial 3 cm channel (no response added) is also shown in the legend of panel e) and f) for HbO and HbR respectively. All concentrations are expressed in micromolar (μM) units.

The summary R^2 statistics over all subjects, all channels and all instances are shown in a bar graph in Fig. 2-4 for both HbO and HbR. These values represent the Pearson R^2 coefficients computed between the recovered and the simulated hemodynamic responses. The bars represent the mean and the error bars represent the standard deviation. Both the mean and the standard deviation were computed on the Fisher transformed values and then inverse transformed. Two-tailed paired t-tests on the
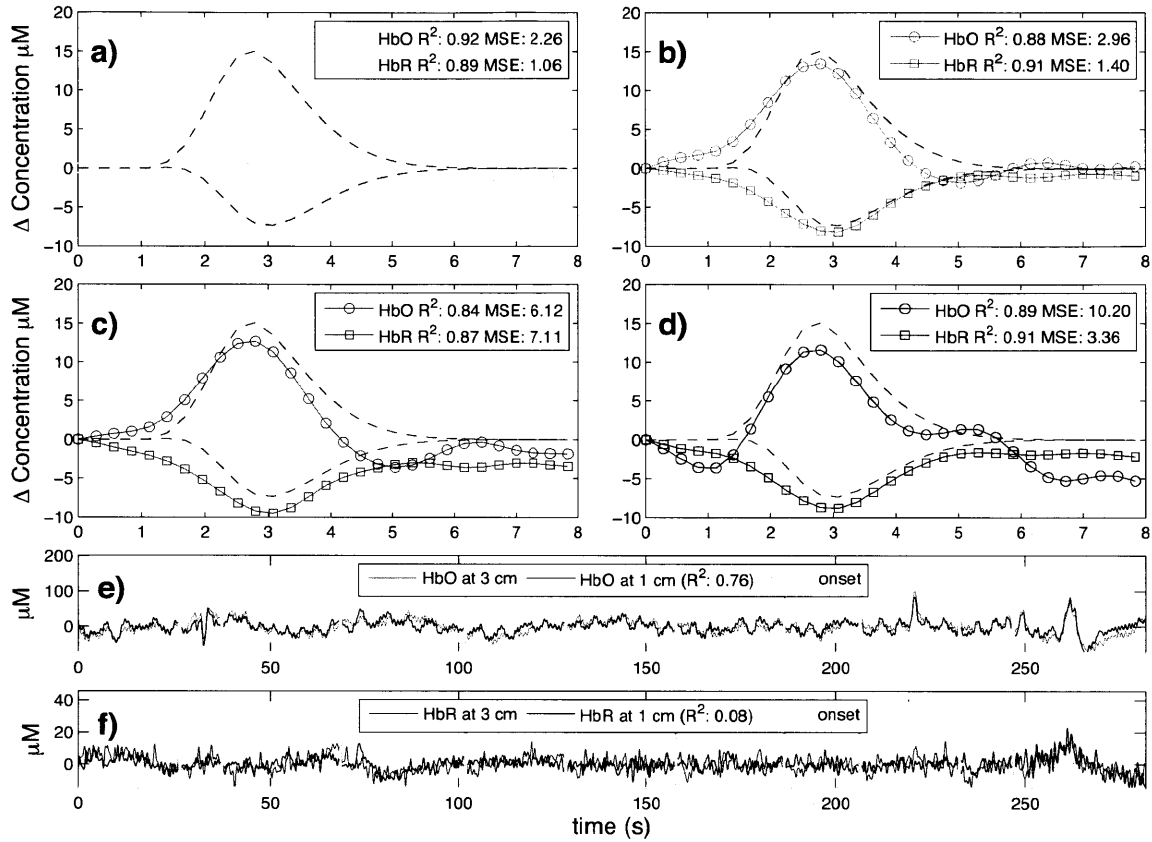
Figure 2-3: a) to d) Typical time courses of the recovered hemodynamic responses overlapped with the simulated hemodynamic response. For these specific traces, the SNR was 0.33 for HbO and 0.81 for HbR. R^2 coefficients and MSEs between the recovered (circles) and the simulated (dashed) response are shown in the legends. a) Kalman filter estimator b) Static estimator c) Adaptive filter d) Standard GLM with 3rd order drift. e) HbO and f) HbR time courses of the 3 cm channel (with synthetic responses added) overlapped with the 1 cm channel. The positions of the onset time are also shown and the correlation coefficients between the 1 cm and the 3 cm channels (before adding synthetic responses) are indicated in parenthesis.

Fisher transformed values were performed between all the different estimators and statistical significance at the level $p < 0.05$ is illustrated by a black line over the bars for which a significant difference was observed. In our three simulations using 10, 30 and 60 trials respectively, the R^2's for HbO and HbR obtained using our Kalman filter dynamic estimator were significantly higher ($p < 0.05$) than the ones obtained using the adaptive filter. Moreover, the R^2's obtained were higher with the Kalman filter than with the static estimator. These differences were significant ($p < 0.05$) except in our 10 trial simulation for HbO.

Similarly, the summary MSE statistics over all subjects, all channels and all instances are shown in Fig. 2-5. These values represent the mean square error computed between the recovered and the simulated hemodynamic responses. The bars represent the mean while the error bars represent the standard deviation. Two-tailed paired t-tests were performed between all the different estimators and statistical significance at the level $p < 0.05$ is illustrated by a black line over the bars for which a significant difference was observed. The MSEs obtained for HbO and HbR in our three simulations (10, 30 and 60 trials) were significantly lower ($p < 0.05$) with our Kalman filter estimator than with the adaptive filter. Futhermore, the MSEs obtained with the Kalman filter were also lower ($p < 0.05$) than the ones obtained with the static estimator for both HbO and HbR in our three simulations.

Table 2.1 summarizes the statistical analysis over all the subjects, all the channels and all the instances for both HbO and HbR and for the simulations with 10, 30 and 60 trials. Each algorithm was compared to every other. The values shown are the p-values obtained from a two-tailed paired t-test. Statistical differences at the level $p < 0.05$ are indicated with bold script. These p-values were computed from the data summarized in the bar graphs shown in Figs. 2-4 and 2-5.

31

Figure 2-4: Pearson R^2 coefficients between simulated and recovered hemodynamic responses. The bars represent the means and the error bars represent standard deviations computed accross all subjects, all channels and all intances. The means and the standard deviation were computed in the Fisher space and then inverse transformed. Two-tailed paired t-tests were performed on the Fisher transformed R^2's. Statistical differences ($p < 0.05$) between the four algorithms are indicated by black horizontal lines over the corresponding bars.

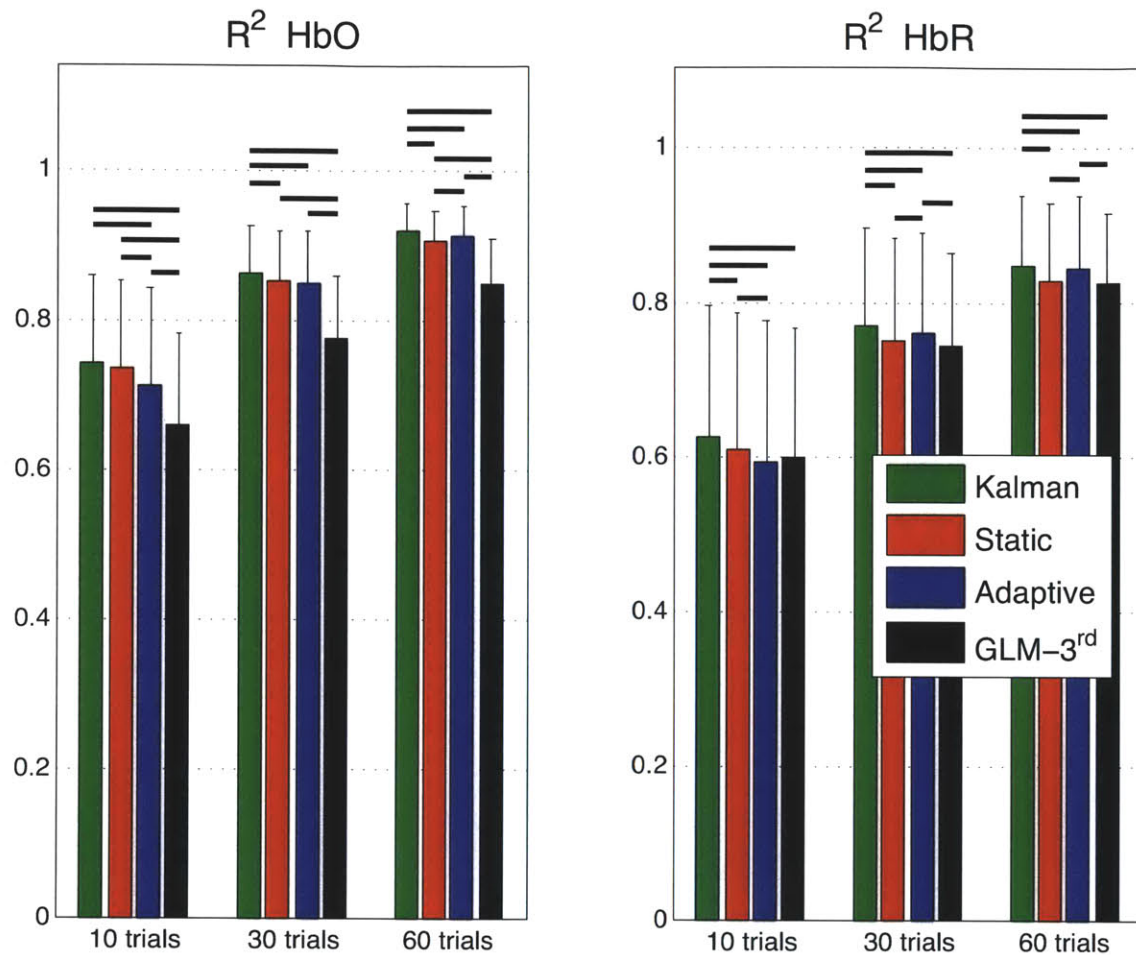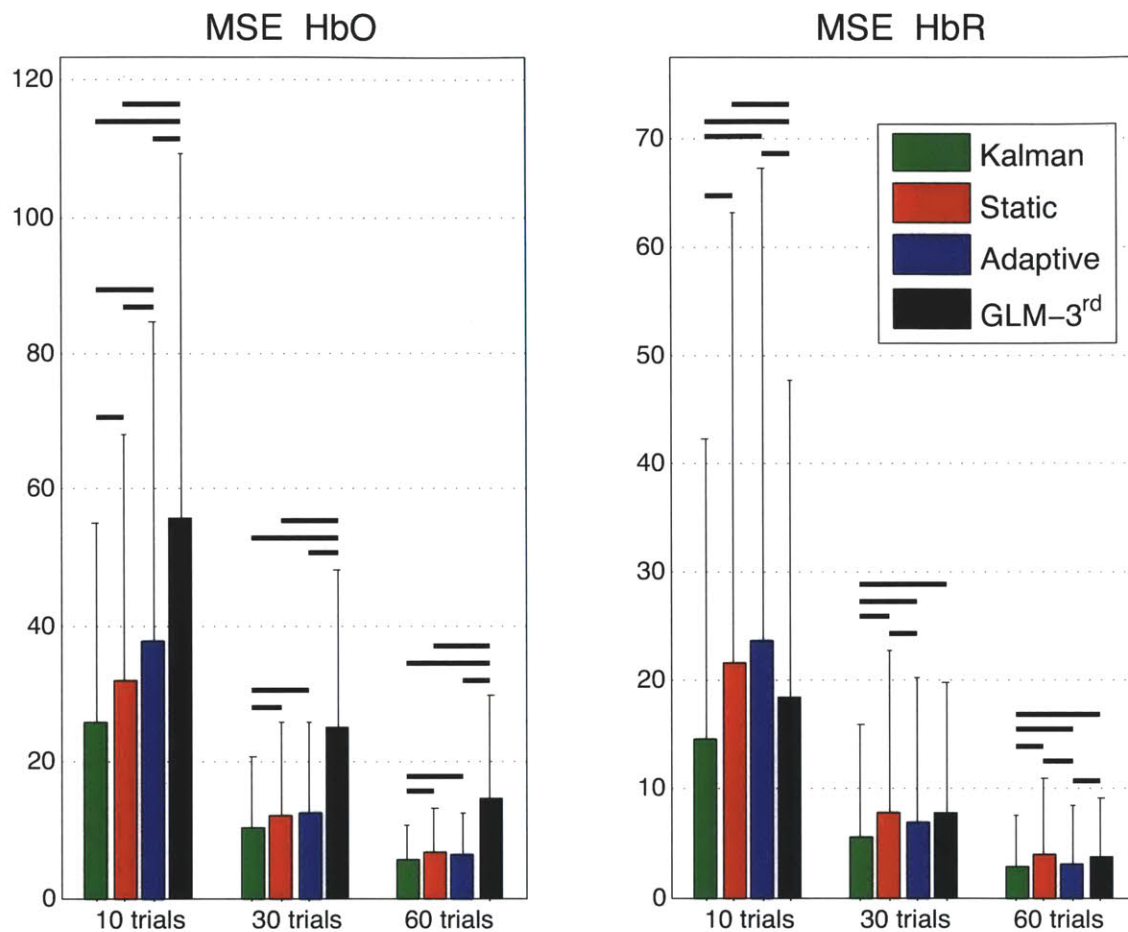Figure 2-5: Mean squared errors (MSE) between simulated and recovered hemodynamic responses. The bars represent the means and the error bars represent the standard deviations computed accross all subjects, all channels and all instances. Two-tailed paired t-tests were performed between the four estimators and statistical differences at the level $p < 0.05$ are indicated by black horizontal lines over the corresponding bars.

Table 2.1: Cross-comparison of the different algorithms. P-values for the two-tailed paired t-tests accross all subjects, all channels and all intances are shown. For the R^2 coefficients, the tests were performed on the Fisher transformed values. **Bold face** indicates significant difference at the $p < 0.05$ level. KF: Kalman filter estimator, SE: Static estimator, AF: Adaptive filter, GLM: Standard GLM with 3rd order drift.

	10 trials			30 trials			60 trials		
	KF	SE	AF	KF	SE	AF	KF	SE	AF
R^2 HbO									
SE	6e-02	-	-	**3e-03**	-	-	**2e-07**	-	-
AF	**2e-07**	**6e-06**	-	**1e-03**	5e-01	-	**4e-04**	**2e-03**	-
GLM	**3e-15**	**2e-13**	**4e-07**	**8e-16**	**2e-12**	**4e-13**	**6e-15**	**1e-10**	**5e-14**
R^2 HbR									
SE	**5e-05**	-	-	**2e-09**	-	-	**1e-08**	-	-
AF	**2e-07**	**2e-03**	-	**3e-05**	**5e-03**	-	**4e-02**	**6e-10**	-
GLM	**5e-04**	2e-01	4e-01	**7e-04**	3e-01	**4e-02**	**1e-04**	6e-01	**7e-04**
MSE HbO									
SE	**4e-06**	-	-	**3e-05**	-	-	**4e-06**	-	-
AF	**2e-05**	**7e-03**	-	**1e-06**	7e-01	-	**2e-05**	6e-02	-
GLM	**2e-12**	**2e-09**	**5e-05**	**1e-13**	**7e-11**	**1e-11**	**4e-10**	**3e-08**	**2e-09**
MSE HbR									
SE	**2e-05**	-	-	**4e-05**	-	-	**1e-04**	-	-
AF	**3e-05**	2e-01	-	**2e-04**	**4e-03**	-	**7e-03**	**7e-05**	-
GLM	**6e-08**	**3e-02**	**1e-02**	**3e-07**	9e-01	9e-02	**4e-06**	1e+00	**5e-04**

2.3 Discussion

2.3.1 Simultaneous filtering and estimation

One of the salient features of our Kalman filter estimator is that it filters the global interference and simultaneously estimates the hemodynamic response. This feature resulted in a more accurate recovery of the hemodynamic response with our Kalman filter estimator compared to the adaptive filter, for which the filtering and the estimation were performed in two distinct steps. Independent regression of the small separation channel potentially removes contributions of the hemodynamic response in the signal which lead to an underestimation of the hemodynamic response thereafter. Our Kalman filter estimator avoids this pitfall. Compared to the adaptive filter, our Kalman filter estimator showed significant improvements at the $p < 0.05$ level in both HbO and HbR recoveries for our 10, 30 and 60 trial simulations. Those improvements were observed in both Pearson R^2 and MSE metrics.

2.3.2 Dynamic versus static estimation

The systemic interference present in NIRS data is non-stationary. This has been nicely shown by Lina et al [33] who performed a detailed wavelet analysis of resting NIRS data with blood pressure, respiratory and heart rate data acquired simultaneously on awake human subjects. The amplitude of the systemic physiology measured by the 1 cm and the 3 cm channel depends on the respective pathlength of the light for each channel. Systemic physiology could alter the optical properties of the tissue over time. As a result, a sustained change in absorption could modify the pathlength of the light independently in the 1 cm and the 3 cm channel, modifying at the same time the relative amplitude of the systemic physiology detected in each channel. This feature of the systemic interference explains why our Kalman filter, which is a dynamic estimator, performed better than the static estimator. Using our Kalman

filter estimator, improvements in the HbO and HbR recovery were observed in both the Pearson R^2 and the MSE metrics compared to the static estimator. All these improvements were significant at the $p < 0.05$ level except for the HbO Pearson R^2 improvement which was not significant in our 10 trial simulation.

2.3.3   HbO versus HbR

In their wavelet analysis, Lina et al [33] also showed that the HbO time courses were more contaminated by global interference than the HbR time courses. As such, the correlation between the 1 cm and 3 cm channel should be higher for HbO than HbR, and filtering methods using 1 cm SD separations should work better for HbO than for HbR. In our data, the mean initial Pearson R^2 correlation between the 1 cm and 3 cm signals were higher for HbO than HbR (0.47 vs 0.22). Comparing our Kalman filter estimator with the standard block average estimator, the p-values obtained in the t-tests performed on the Fisher transformed Pearson R^2's and the MSEs were at least five orders of magnitude lower for HbO than HbR. This indicates that the improvements observed with our Kalman filter were more prominent for HbO than HbR. This better performance in the recovery of HbO over HbR using a small separation method was also reported by Zhang et al [51] using their adaptive filter.

2.3.4   Impact of initial correlation

In the case where the systemic physiology present in the 3 cm separation did not correlate with the systemic physiology present in the 1 cm channel, the performance of the Kalman filter was similar to the standard GLM. In this case, the model cannot reproduce the data and the a_i coefficients in Eq. 3.2 converge to zero. As such, the w_i's estimated by the Kalman filter are very close to the ones obtained using the GLM. An important point is that in the case of low initial R^2 coefficients ($0.1 < R^2 < 0.2$), taking into account the 1 cm channel with the Kalman filter did not

decrease the performance of the recovery compared to the GLM. On the other hand, the performance of the adaptive filter for (0.1 < initial R^2 < 0.2) was worst than the GLM. This counter-performance of the adaptive filter for poor initial correlation between the short and the long channel was also reported by Zhang et al [51]. These findings suggest that the Kalman filter can be used even if the correlation between the 1 cm and the 3 cm channel is low as opposed to the adaptive filter. In the worst case, the Kalman filter will be as good as the standard GLM. However, the higher the initial correlation between the 1 cm and the 3 cm channel is, the more significant is the improvement using a small separation measurement. This is illustrated by the larger improvement obtained for HbO than HbR when using a small separation measurement together with our Kalman filter.

2.3.5   Technical notes

The MSEs obtained in our simulations and presented in Fig. 2-5 were lower for HbR than HbO. This occurred because the amplitude of the simulated HbR response was lower than the simulated HbO response which resulted in lower MSEs for HbR. This is illustrated for noise-free data in Fig. 2-2b.

For all the results presented in this paper, a single time point was taken from the 1 cm channel to regress the 3 cm channel. In practice, this value could be any integer. A simple phase shift (delay) between the 3 cm and 1 cm channel would be taken into account by using multiple time points from the 1 cm. In this case, all the a's in Eq. 3.2 would converge to zero except for one a at the value of i corresponding to the shift between the two signals in terms of number of sample points. Different values for N_a were tested during our simulations. With the adaptive filter, we obtained better results using a single point than using 100 points as in Zhang et al [52]. Using 100 points results in overfitting the signal which removes more of the hemodynamic response contribution than using a single point. This is another pitfall of the non-simultaneous recovery and filtering feature of the adaptive filter which is avoided with

our Kalman filter. Finally, we did not observe any improvement when using multiple points with our Kalman filter, suggesting that no delays were present in our data between the 1 cm and the 3 cm channel.

The Gaussian temporal basis functions used in this work allow us to model different hemodynamic responses with different shapes and components. This includes a potential initial dip and post-stimulus undershoot, responses with a double bump and negative responses. It is also easy to use additional Gaussian functions to extend this method for longer stimuli, making the temporal basis set used in the present work very general and less restrictive. However, as stated in section 2.1.3, the drawback for using a more general set is the potential overfitting of phase-locked systemic physiology. This could be avoided using a more restrictive temporal basis set such as a gamma-variant function and its derivatives [24, 1, 21, 14], and at the same time could potentially reduce the number of parameters to estimate.

We tested different values for the separation between the basis and also different values for the width of the Gaussians. The values of 0.5 second for both the separation and the width presented in this paper resulted in the lowest MSEs between the recovered and the simulated responses and highest R^2's. The separation between our temporal basis Gaussians and their widths was three times lower than the values used by Diamond et al [7].

In order to compare the four methods used in this work on the same footing, we used temporal basis functions for each estimator. For the standard GLM estimator, the adaptive filter and the Kalman filter, we have also tried to replace the final step of using the GLM with a temporal basis set by a simple block average without using any temporal prior. For all these three estimators, using temporal basis functions in the final step further improved the recovery of both HbO and HbR. The MSEs between the recovered and the simulated hemodynamic response were lower when temporal basis were used than when a simple block average without temporal basis was applied. Similarly, the R^2's computed between the recovered and the simulated

responses were higher when temporal basis were used in the final block average step. This result raises the importance of using temporal priors to reduce the dimensionality of the estimation problem.

As stated in section 2.1.7, changing the state process noise and the measurement noise priors over two orders of magnitude did not affect the performance of our Kalman estimator. For HbO, no differences could be observed (two-tailed paired t-test, $p < 0.05$) between the MSEs recovered using values for the process noise or the measurement noise ten times lower or higher than the ones presented in section 2.1.7. For HbR, small differences in the MSEs were observed but these results did not change any conclusions drawn in this paper. The MSEs recovered with our Kalman filter in this case were still the lowest of the four estimators.

2.3.6 Future directions

As mentioned in Zhang et al [51], an important question is whether an additional short separation optode is required for each longer separation optode or whether a single one is sufficient. Although the systemic interference is thought to be global in the brain, it might be reflected differently in the NIRS data collected over different regions of the head. Sources of variation include blood vessel size which might affect the amplitude of the recovered response but also blood vessel length and geometry which might give rise to phase mismatches between different NIRS channels. Studies using multiple small SD separation optodes at different locations over the head should be performed in the future to address this question.

2.4 Summary

In summary, we filtered the global interference present in NIRS data by using additional small separation optodes and we simultaneously estimated the hemodynamic

response using a dynamic algorithm. Our dynamic Kalman filter performed better than the traditional adaptive filter, the static estimator and the standard block average estimator for both HbO and HbR recovery. These results were consistent with the fact that dynamic estimation better captures the non-stationary behavior of the systemic interferences in NIRS and that the simultaneous filtering and estimation prevents underestimation of the hemodynamic response. The algorithm is easily implementable and suitable for a wide range of NIRS studies.

2.5   Appendix: Design matrix

The explicit expression for $\mathbf{D}$ in Eq. 2.9 is given by

$$\mathbf{D} = \begin{bmatrix} 1 & 1/N_t & 1^2/N_t^2 & 1^3/N_t^3 \\ 1 & 2/N_t & 2^2/N_t^2 & 2^3/N_t^3 \\ 1 & 3/N_t & 3^2/N_t^2 & 3^3/N_t^3 \\ \vdots & \vdots & \vdots & \vdots \\ 1 & N_t/N_t & N_t^2/N_t^2 & N_t^3/N_t^3 \end{bmatrix}.$$

The dimension of the matrix $\mathbf{D}$ is N_r by 4. Each column is normalized by its highest value to keep the matrix $\mathbf{G}$ well conditioned and to avoid numerical errors during the inversion in Eq.2.10.

The explicit expression for $\mathbf{A}$ in Eq. 2.17 is given by

$$
\mathbf{A} =
\begin{bmatrix}
b_1[1] & b_2[1] & \dots & b_{N_w}[1] & y_1[1] & 0 & \dots & 0 \\
b_1[2] & b_2[2] & \dots & b_{N_w}[2] & y_1[2] & y_1[1] & & 0 \\
\vdots & \vdots & & \vdots & \vdots & \vdots & \ddots & \vdots \\
b_1[N_b] & b_2[N_b] & \dots & b_{N_w}[N_b] & \vdots & \vdots & & y_1[1] \\
0 & 0 & & 0 & \vdots & \vdots & & \vdots \\
\vdots & \vdots & & \vdots & \vdots & \vdots & & \vdots \\
0 & 0 & & 0 & \vdots & \vdots & & \vdots \\
b_1[1] & b_2[1] & \dots & b_{N_w}[1] & \vdots & \vdots & & \vdots \\
b_1[2] & b_2[2] & \dots & b_{N_w}[2] & \vdots & \vdots & & \vdots \\
\vdots & \vdots & & \vdots & \vdots & \vdots & & \vdots \\
b_1[N_b] & b_2[N_b] & \dots & b_{N_w}[N_b] & \vdots & \vdots & & \vdots \\
0 & 0 & & 0 & \vdots & \vdots & & \vdots \\
\vdots & \vdots & & \vdots & \vdots & \vdots & & \vdots \\
\vdots & \vdots & & \vdots & y_1[N_t] & y_1[N_t-1] & \dots & y_1[N_t - N_a + 1]
\end{bmatrix}.
$$

N_b is the length of each temporal basis function and was 80 in our work due to the 10 Hz temporal resolution and 8 s FIR for our temporal basis functions. The vertical dimension of matrix $\mathbf{A}$ corresponds to N_t, the total number of time points in the entire time course. The number of copies of the temporal basis functions corresponds to the number of trials (or stimuli) in the specific time course (i.e. if the run contained 10 trials, then 10 copies of the temporal basis set will appear in the corresponding $\mathbf{A}$ matrix).

Chapter 3

Impact of the short channel location

This section was submitted for publication:

Gagnon, L., Cooper, R. J., Yucel, M. A., Perdue, K., Greve, D. N., and Boas, D. A. (2011). "Short separation channel location impacts the performance of short channel regression in NIRS." *submitted*

The main contribution of this chapter is to quantify the performance of the short separation method as a function of the relative distance between 3 cm NIRS channels containing the brain signal and 1 cm channels used as a regressors. We investigated this relationship with both simulations and real functional data. NIRS measurements including several short separation channels spread across the probe were acquired on 6 human subjects. The simulations were performed by adding a synthetic hemodynamic response to the resting-state NIRS data. NIRS signals were also collected during a series of finger tapping blocks for each of the 6 subjects. In both cases, the performance of the short separation regression was characterized for different short SD regressors located at different distances from the standard 3 cm channel.

3.1 Methods

3.1.1 Experimental data

For this study, 6 healthy adult subjects were recruited. The Massachusetts General Hospital Institutional Review Board approved the study and all subjects gave written informed consent. Data were collected using a TechEn CW6 system operating at 690 and 830 nm. The NIRS probe contained 5 sources and 12 detectors as shown in Fig. 3-1a. This source-detector geometry resulted in 14 long SD measurements (3 cm) and 7 short SD measurements (1 cm). A set of 200 μm-core fibers was used for the short separation detector optodes to avoid saturation of the photodiode. These fibers are illustrated in orange in Fig. 3-1. An alternative to avoid photodiode saturation could be the use of standard NIRS fibers with optical filters at the tip of the probe to attenuate light intensity. The probe was secured over the left motor region of each subject as illustrated in Fig. 3-1b. One of the 1 cm measurements was acquired over the forehead. In this probe, the relative distances center-to-center between the short and the long channels could take the values 1.4, 1.7, 2.4, 3.3, 4.2, 5.2 or 6.2 cm. Examples are given for each case in Fig. 3-1c. The forehead short channel was located more than 10 cm away from any 3 cm channel.
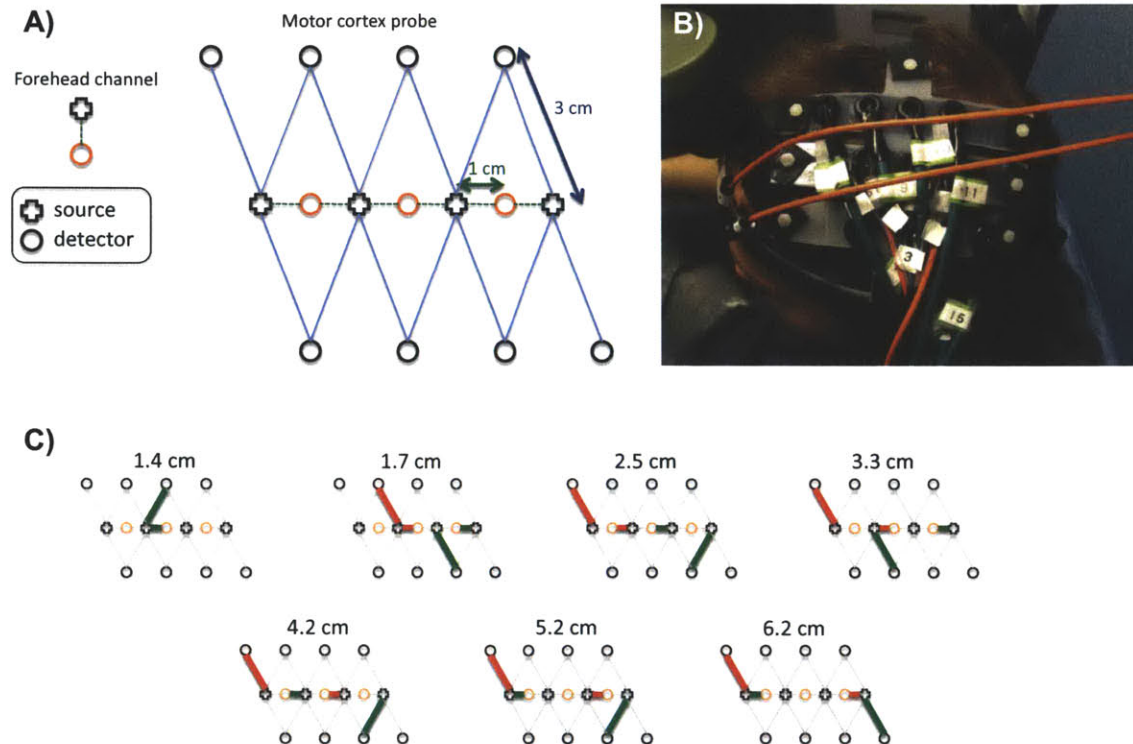
Figure 3-1: (A) Geometry of the optical probe. Two different SD separations were used: 1 cm and 3 cm. (B) Location of the probe on the subjects. The probe was secured over the motor region. (C) Examples of short and long channel pairs. With this probe arrangement, the possible relative distances between the short and the long SD channels were 1.4, 1.7, 2.5, 3.3, 4.2, 5.2 and 6.2 cm.

During the experiment, subjects were sitting in a comfortable chair in front of a computer screen with a black background. The functional runs were divided as shown in Fig. 3-2. Each run lasted 390 seconds and contained six blocks of 30 s finger tapping interleaved with 30 s resting blocks. Three functional runs were acquired for each subject. During the resting blocks, a small 0.5-by-0.5 cm white square located at the middle of the screen appeared and the subjects were asked to fixate on this square. During the finger tapping blocks, the instruction "tap your fingers" was displayed in white characters on the computer screen using the Psychophysics toolbox in Matlab [3]. At that time, the subjects were asked to touch their right thumb with each of the fingers of their right hand alternately at a rate of 3 Hz. Following the three functional runs, three baseline runs of 5 minutes each were acquired. During the baseline runs, the subjects were asked to simply close their eyes and remain still.
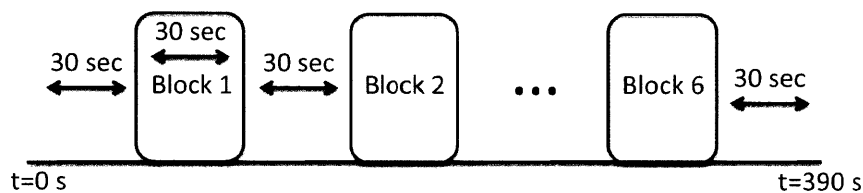

Figure 3-2: Overview of the finger tapping protocol. A run consisted of 6 blocks of 30 seconds of finger tapping interleaved with 30 seconds of rest. Each runs started and ended with a 30 second resting period. 3 functional runs were acquired for each of the 6 subjects.

3.1.2 Data processing

An overview of the procedure is shown in Fig. 3-3. Both the short and long SD measurements were bandpass filtered at 0.01-1.25 Hz. For both the simulations and the real functional data analysis, our Kalman filter algorithm was used to regress the short separation measurement and recover the hemodynamic response simultaneously. This algorithm was described in detail previously [11] and only the salient points are reviewed here.

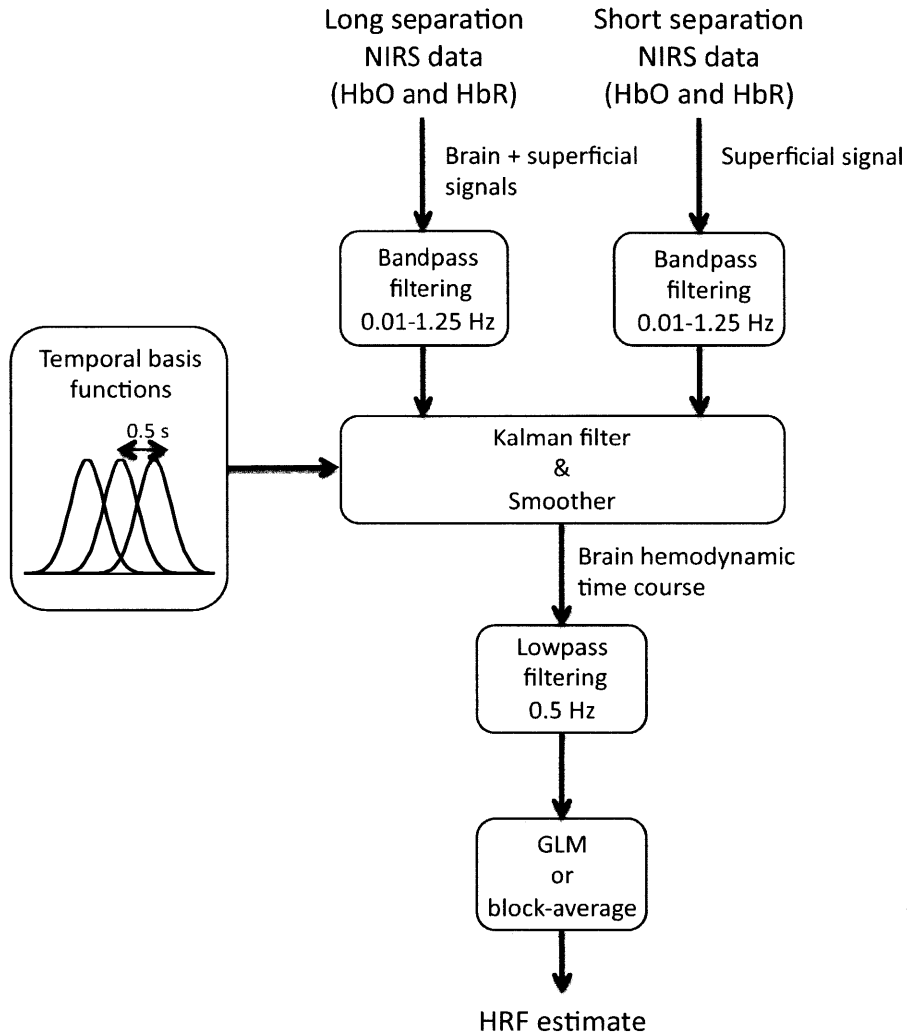Figure 3-3: Schematic of the NIRS data analysis. The NIRS data from both the 1 cm and the 3 cm separation channels were first converted to HbO and HbR time courses and bandpass filtered. HbO and HbR were analyzed separately. The 1 cm and 3 cm bandpass time courses were passed to the Kalman algorithm [11] and then further lowpass filtered. The HRF was finally estimated using the GLM or a standard block-average.

The hemodynamic response was modeled by

$$h[n] = \sum_{i=1}^{N_w} w_i b_i[n].$$ (3.1)

where $b_i[n]$ are normalized Gaussian functions with a standard deviation of 0.5 s and their means separated by 0.5 s. N_w is the number of Gaussian functions used to model the hemodynamic response and was set to 15 for our simulations (section 3.1.3) and 79 for our finger tapping data to recover the HRF over 0-8 sec and 0-40 sec respectively. The signal in the 3 cm separation channel $y_3[n]$ was modelled by a linear combination of the 1 cm separation signal $y_1[n]$ and the hemodynamic response $h[n]$. The expression for the 3 cm signal is given by

$$y_3[n] = \sum_{k=-\infty}^{\infty} h[k] u[n-k] + a\, y_1[n].$$ (3.2)

The variable a is the dynamic weight used to model the superficial signal in the 3 cm separation channel from the linear combination of the 1 cm separation signal. Only a single time delay was taken from the 1 cm channel to model the superficial signal in the 3 cm channel since this has been shown to result in a better performance in our previous paper [11]. The states to be estimated by the Kalman filter were the weight of the superficial contribution a and the weights of the temporal bases w_i. All these weights were assumed to be time-varying. Eqs. 3.1 and 3.2 can be re-written in state-space form:

$$\mathbf{x}[n+1] = \mathbf{I}\mathbf{x}[n] + \mathbf{w}[n]$$ (3.3)

$$y_3[n] = \mathbf{C}[n]\mathbf{x}[n] + \mathbf{v}[n]$$ (3.4)

where $\mathbf{w}[n]$ and $\mathbf{v}[n]$ are the process and the measurement noise respectively. $\mathbf{x}[n]$ is the nth instance of $\mathbf{x}$ given by

$$\mathbf{x} = \begin{bmatrix} w_1 & \dots & w_{N_w} & a \end{bmatrix}^T.$$ (3.5)

The quantity $\mathbf{I}$ is an $N_w + 1$ by $N_w + 1$ identity matrix and $\mathbf{C}[n]$ is a 1 by $N_w + 1$ vector given by

$$\mathbf{C}[n] = \begin{bmatrix} u * b_1[n] & \cdots & u * b_{N_w}[n] & y_1[n] \end{bmatrix} \tag{3.6}$$

with $u[n]$ the onset vector which is a binary vector taking the value 1 when n corresponds to a time when the stimulus was presented and 0 otherwise. The estimate $\hat{\mathbf{x}}[n]$ at each sample n is then computed using the Kalman filter [31] followed by the Rauch–Tung–Striebel smoother [40].

The initial state vector estimate $\hat{\mathbf{x}}[0]$ was set to the values obtained using a static estimator as in [11] and the initial state covariance estimate $\mathbf{P}[0]$ was set to an identity matrix with diagonal entries of $1\text{x}10^{-1}$ for the temporal basis states and $5\text{x}10^{-4}$ for the superficial contribution state. The Kalman filter algorithm was run twice and the initial covariance estimate for the second run was set to the final covariance estimate of the first run. The process noise covariance $\mathbf{Q}$ only contained nonzero terms on the diagonal elements. Those diagonal terms were set to $2.5\text{x}10^{-6}$ for the temporal basis states and $5\text{x}10^{-6}$ for the superficial contribution state. The measurement noise covariance $\mathbf{R}$ was set to an identity matrix scaled by $5\text{x}10^{-2}$. The Kalman filter algorithm was then processed with the following prediction-correction recursion [12]:

$$\hat{\mathbf{x}}[n|n-1] = \hat{\mathbf{x}}[n-1|n-1] \tag{3.7}$$

$$\hat{\mathbf{P}}[n|n-1] = \hat{\mathbf{P}}[n-1|n-1] + \mathbf{Q}. \tag{3.8}$$

$$\mathbf{K}[n] = \hat{\mathbf{P}}[n|n-1]\mathbf{C}[n]^T \left(\mathbf{C}[n]\hat{\mathbf{P}}[n|n-1]\mathbf{C}[n]^T + \mathbf{R}\right)^{-1} \tag{3.9}$$

$$\hat{\mathbf{x}}[n|n] = \hat{\mathbf{x}}[n|n-1] + \mathbf{K}_n \left(y_3[n] - \mathbf{C}[n]\hat{\mathbf{x}}[n|n-1]\right) \tag{3.10}$$

$$\hat{\mathbf{P}}\left[n|n\right] = \left(\mathbf{I} - \mathbf{K}\left[n\right]\mathbf{C}\left[n\right]\right)\hat{\mathbf{P}}\left[n|n-1\right]. \tag{3.11}$$

After the Kalman algorithm was applied twice, the Rauch–Tung–Striebel smoother was applied in the backward direction [18]:

$$\hat{\mathbf{x}}\left[n|N_t\right] = \hat{\mathbf{x}}\left[n|n\right] + \hat{\mathbf{P}}\left[n|n\right]\hat{\mathbf{P}}\left[n+1|n\right]^{-1}\left(\hat{\mathbf{x}}\left[n+1|N_t\right] - \hat{\mathbf{x}}\left[n+1|n\right]\right) \tag{3.12}$$

with N_t the number of time points in the data. The complete time course of the estimated hemodynamic response $\hat{h}\left[n\right]$ was then reconstructed for each sample time n using the final state estimates $\hat{\mathbf{x}}\left[n|N_t\right]$ and the temporal basis set contained in $\mathbf{C}\left[n\right]$

$$\hat{h}\left[n\right] = \mathbf{C}\left[n\right]\hat{\mathbf{x}}\left[n|N_t\right]. \tag{3.13}$$

This reconstructed hemodynamic response time course $\hat{h}\left[n\right]$ was further lowpass filtered at 0.5 Hz and the final estimate of the hemodynamic response was obtained by applying the standard GLM as in [11].

3.1.3   Simulations

For each baseline measurement, the changes in optical density were converted to changes in hemoglobin concentrations using the modified Beer-Lambert relationship [4, 6, 2]. A pathlength correction factor of 6 and a partial volume correction factor of 50 were applied [26, 27]. The variance in all 252 (6 subjects x 3 runs x 14 pairs) baseline HbO and HbR time courses from the 3 cm measurements were then computed. To ensure a uniform distribution of the noise in our simulations, only the time courses showing a variance below 25 μM^2 were kept in the analysis, corresponding to 28.2 % of the data (71 of the 252 baseline time courses).

Ten individual evoked responses were added over all 71 selected 3 cm baseline measurements at random onset times with an inter-stimulus interval taken randomly from

a uniform distribution (10-30 sec). This procedure was repeated 30 times for each baseline measurement to create 30 simulated time courses with 30 different onset times and ensure reproducible averaged results. The duration of the synthetic response was 8 seconds. The HbO time course increased by 15 μM at the peak while the HbR time course decreased by 7 μM. The synthetic hemodynamic response was the same used in our previous paper [11]. The resulting 2130 time courses (71 time courses x 30 simulated runs) were then bandpass filtered (0.01-1.25 Hz) and passed to the Kalman filter algorithm (Fig. 3-3) using each of the seven 1 cm measurements available as a regressor. The HRF was also recovered using a standard GLM with a 3rd order polynomial drift for comparison (no short separation used). This resulted in 17,040 estimated HRFs (2130 time courses x 8 regressors (7 short separations + 1 standard GLM with 3rd order polynomial drift)). The HbO and HbR responses were recovered independently. For each 1 cm-3 cm combination, the baseline R^2 coefficient before adding the synthetic HRF to the 3 cm channel was computed.

For each short separation used, the relative center-to-center distance between the 3 cm and the 1 cm channel was computed. With the probe shown in Fig. 3-1a, the possible relative distances are 1.4, 1.7, 2.4, 3.3, 4.2, 5.2 or 6.2 cm as well as > 10 cm for the forehead channel (label "forehead" in our results) and are illustrated in Fig. 3-1c.

The quality of each recovered HRF was quantified by three different metrics: (1) the Pearson correlation coefficient R^2 between the true synthetic HRF (tHRF) and the recovered HRF (rHRF), (2) the mean square error (MSE) between tHRF and rHRF and (3) the Contrast-to-noise ratio (CNR) defined as the amplitude of rHRF divided by the standard deviation of the residual of tHRF and rHRF

$$CNR = \frac{\max{(rHRF)}}{std{(rHRF - tHRF)}}. \tag{3.14}$$

The average for each of these three metrics across all the recovered HRFs for each specific relative distance was computed and the results were compared to the cor-

responding averaged metrics obtained from the HRFs recovered with the standard GLM (no short separation) using a two-tailed paired t-test. As in our previous paper [11], we used a paired t-test to resolve for small systematic differences. For the Pearson R^2 metric, the average was taken after applying a Fisher transformation and the resulting average was then back transformed. This comparison was performed for all 8 relative distances (1.4, 1.7, 2.4, 3.3, 4.2, 5.2, 6.2 cm and forehead),

This entire procedure was then repeated after introducing a time-lag in the short separation channel. For each 1 cm-3 cm combination, the cross-correlation function between the two channels before adding the synthetic HRF was also computed and a time-lag corresponding to the maximum of the cross-correlation function was applied to the short separation measurement. This time-lag could be any number in the interval $\{-N_t, N_t\}$ with N_t the number of time point in the NIRS time course but typical values obtained from our data ranged from -4 to 4 seconds for both HbO and HbR. The values for R^2, MSE and CNR obtained by introducing a time-lag were also compared with the zero-lag values with a two-tailed paired t-test.

The cross-correlation function used to identify the optimal time-lag was normalized such that the zero-lag value corresponded to the Pearson R^2 coefficient

$$\bar{R}_{y_1 y_3}[m] = \frac{R_{y_1 y_3}[m]}{\sigma_{y_1} \sigma_{y_3}} \tag{3.15}$$

with σ_{y_3} the standard deviation of $y_3[n]$. The maximum of this normalized cross-correlation function is the equivalent to shifting one of the channels by the optimal time-lag before computing the standard correlation and thus we will refer to this value as the optimal time-lag correlation for the rest of the text. To avoid any confusion, we will refer to the standard R^2 correlation as the zero-lag correlation. The zero-lag and the optimal time-lag correlations were also compared using a two-tailed paired t-test of their Fisher transformed values.

3.1.4 Functional data

The functional data were analysed in the same way as above with the Kalman filter, but the HRFs were recovered from 0 to 40 seconds after the stimulus onsets. Each 3 cm channel was analyzed using each of the seven short separation channels available and also with a standard block-average for comparison.

3.2 Results

3.2.1 Baseline correlation

The correlation (Pearson R^2) between the baseline NIRS time courses are shown in Fig. 3-4. In the top panels, the correlation between the 3 cm separation and the 1 cm separation channels are plotted as a function of their relative distance on the probe. These values are identified by the label "no time-lag" in the legends. The optimal time-lag correlation values are also plotted and identified by the label "optimum time-lag" in the legends. We observed a decay of both the zero-lag and the optimal time-lag correlations as the distance between the two channels was increased. This decay was observed for both HbO and HbR. The optimal time-lag correlation values obtained were significantly higher ($p < 0.05$, two-tailed paired t-test) than the zero-lag correlation for all relative distances on the probe and for both HbO and HbR. However, the increases in correlation obtained by introducing time-lag were more prominent for HbR than HbO.

In the bottom panel of Fig. 3-4, both the zero-lag and the optimal time-lag correlations between two 1 cm separation channels are plotted as a function of their relative distance on the probe. A similar decay was observed as the relative distance between the two channels increased on the probe. The values for the optimal-time lag correlations in this case were also significantly higher ($p < 0.05$, two-tailed paired t-test)
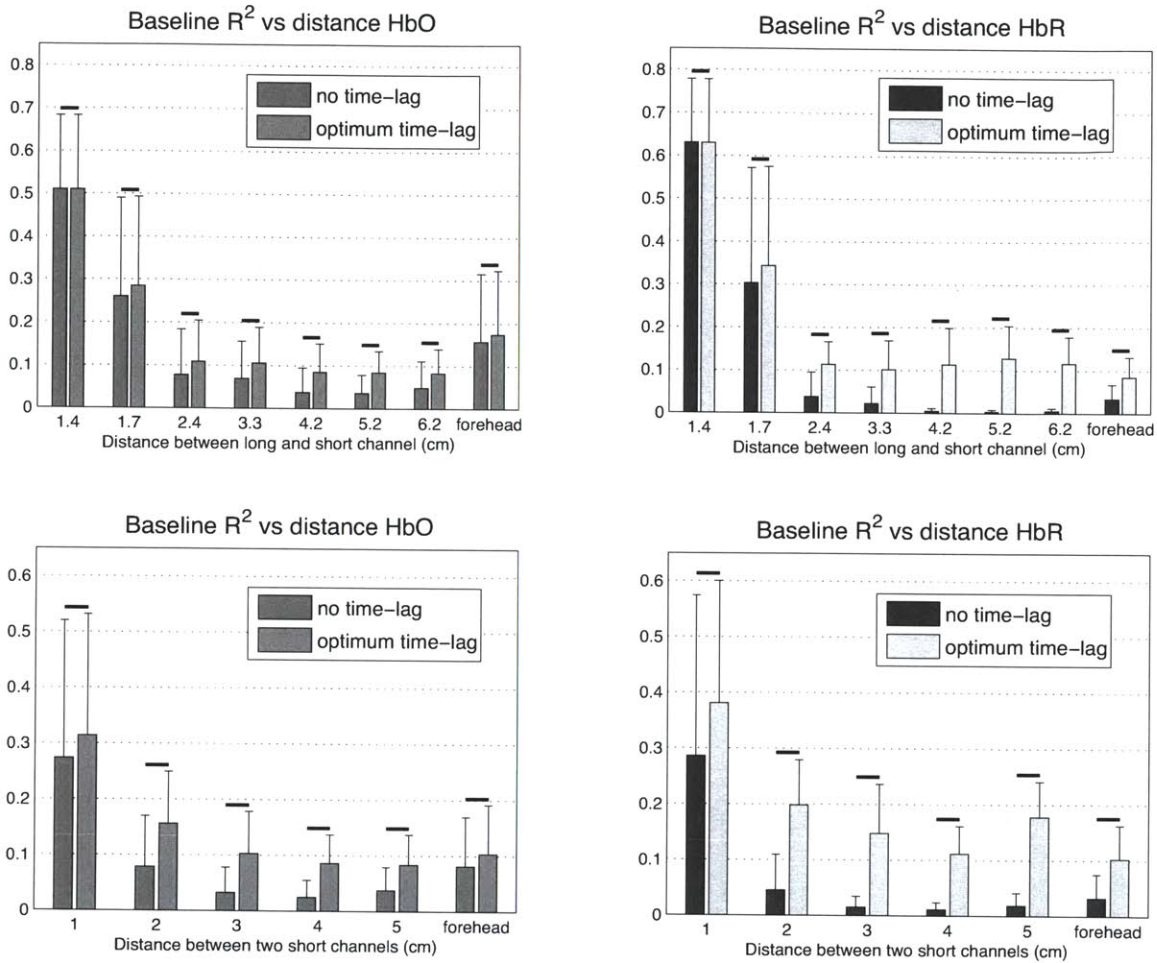
Figure 3-4: Effect of the relative distance on the initial baseline correlation between the channels. The baseline data were bandpass filtered between 0.01 and 1.25 Hz before the R^2 correlation was computed. The values labeled "optimal time-lag" were computed by taking the maximum of the normalized cross-correlation function (Eq. 3.15) while the "no time-lag" values are the standard Pearson R^2 coefficient. Statistical differences at the $p < 0.05$ level are indicate with horizontal black lines (two-tail paired t-test). (Top) Initial baseline R^2 between the long and the short channels as a function of the relative distance between them. (Bottom) Initial baseline R^2 between two short separation channels as a function of the relative distance between them. (left) HbO. (right) HbR.

compared to the zero-lag correlations.

3.2.2   Simulation results

The results for the synthetic HRF simulations are shown in Figs. 3-5, 3-6 and 3-7 for the R^2, MSE and CNR metric respectively. On the top panels of all three figures, the three metrics are plotted as a function of the relative distance between the 3 cm separation and the 1 cm separation channel used as a regressor. Values obtained by introducing a time-lag in the 1 cm separation channel are also shown as well as the corresponding values obtained using a standard GLM for each data subset. We observed a decrease of the improvement obtained by the Kalman filter as the relative distance between the 3 cm and the 1 cm channel was increased. Both the R^2 (Fig. 3-5) and the CNR (Fig. 3-7) decreased as the relative distance between the long and short channels was increased, while the MSE (Fig. 3-6) increased. Using a short separation located 1.4 cm away from the channel containing the synthetic HRF resulted in a mean increase in CNR of 50 % for HbO and 100 % for HbR relative to the GLM method. Using a short separation located farther than 2 cm away from the channel containing the synthetic HRF resulted in significant ($p < 0.05$, two-tailed paired t-test) but negligible improvements of the order of a few percent compared to the standard GLM procedure.

On the bottom panels of Figs. 3-5, 3-6 and 3-7, the same R^2, MSE and CNR results are plotted as a function of the baseline zero-lag correlation (Pearson R^2) between the 3 cm and the 1 cm separation channels. Results obtained by introducing a time-lag in the short separation channel are also plotted as a function of the baseline optimal time-lag correlation. We observed a linear relationship between the improvement obtained with the Kalman filter and both the baseline zero-lag correlations and optimal time-lag correlations between the two channels. A baseline correlation greater than 0.8 resulted in a mean improvement in CNR of 50 % and 100 % compared to the standard GLM for HbO and HbR respectively.
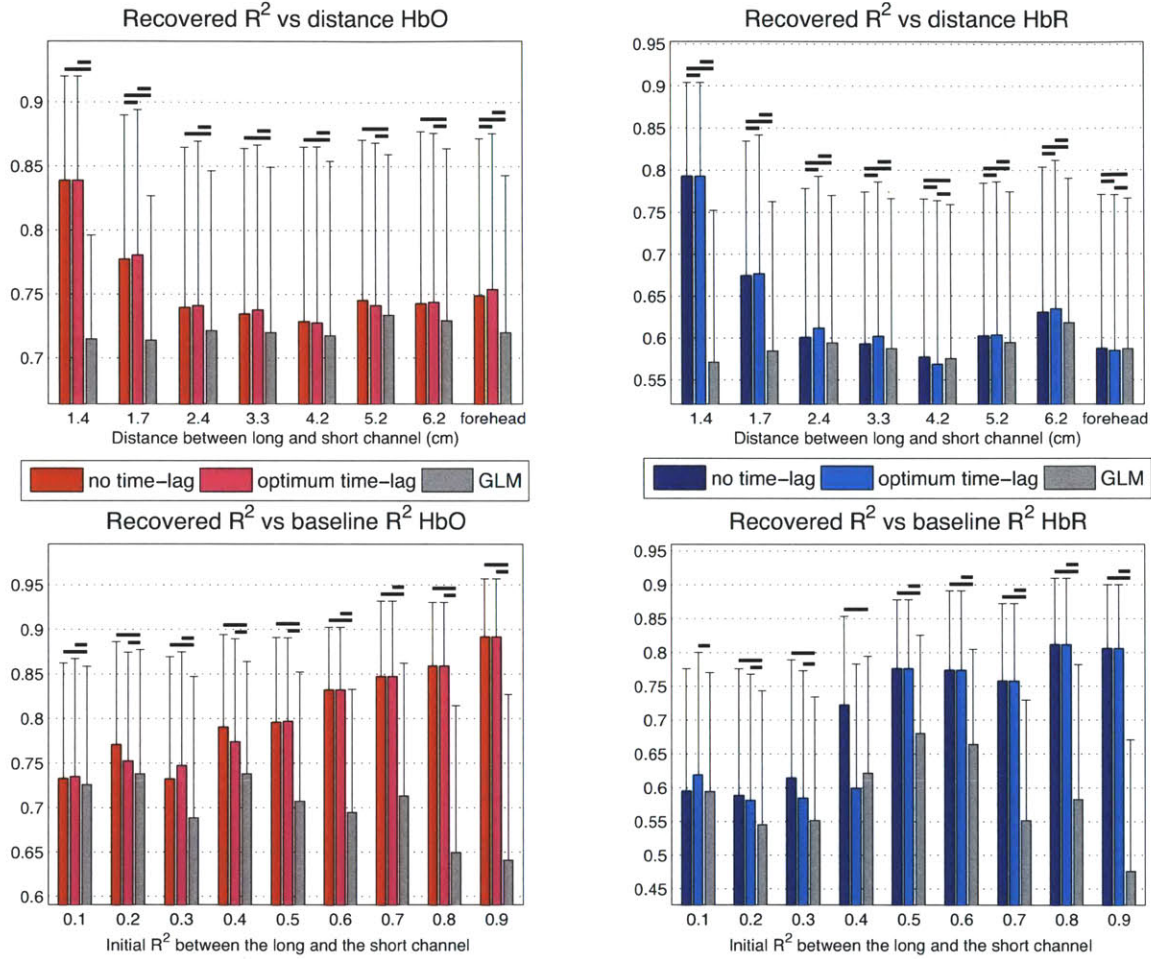
Figure 3-5: Effect of the relative distance on the correlation between the recovered HRF and the true HRF. The top panels show the recovered R^2 as a function of the distance between the short and the long NIRS channel. The bottom panels show the recovered R^2 as a function of the baseline R^2 between the short and the long NIRS channel. The left panels show results for HbO while the right panels show results for HbR. Statistical differences at the $p < 0.05$ level are indicate with horizontal black lines (two-tail paired t-test).
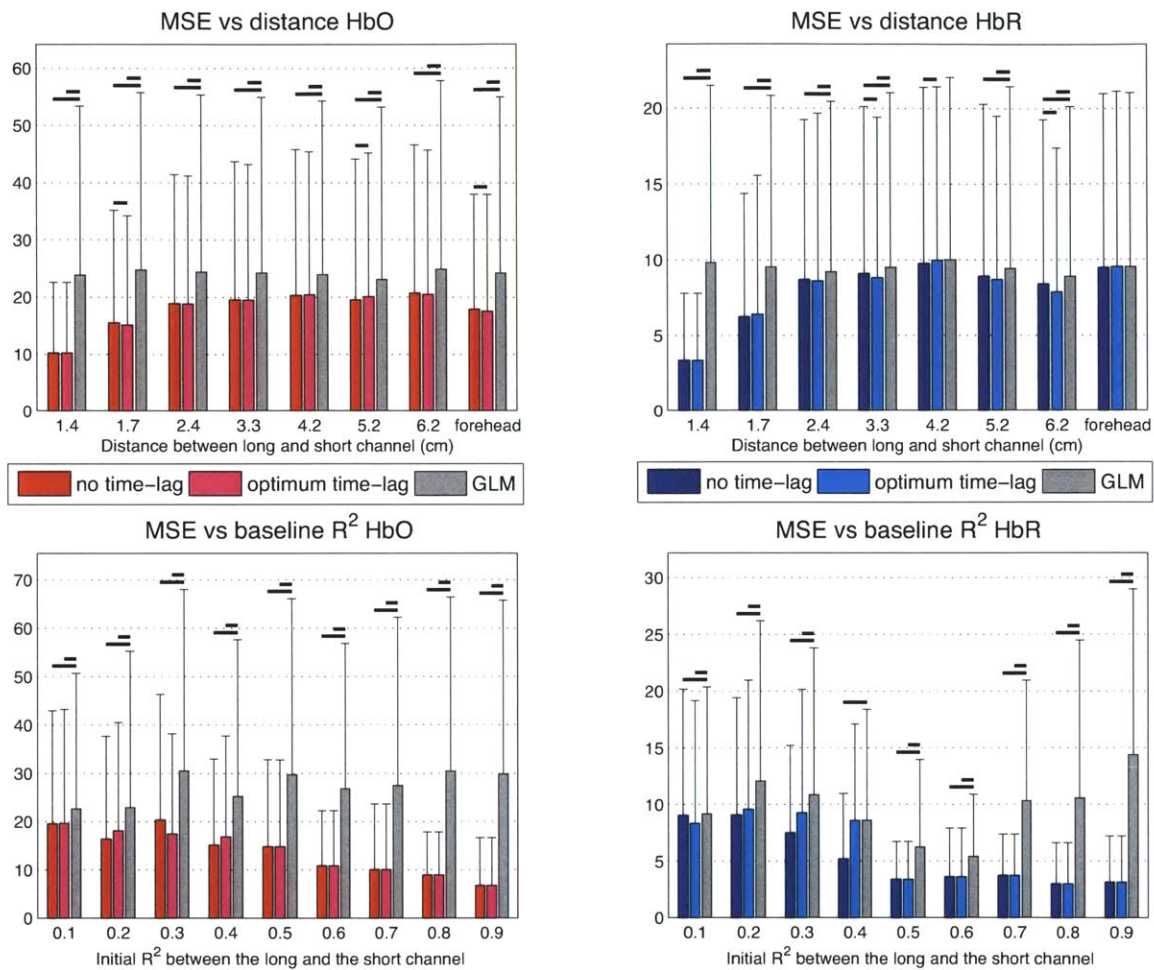
Figure 3-6: Effect of the relative distance on the MSE between the recovered HRF and the true HRF. The top panels show the MSE as a function of the distance between the short and the long NIRS channel. The bottom panels show the MSE as a function of the baseline R^2 between the short and the long NIRS channel. The left panels show results for HbO while the right panels show results for HbR. Statistical differences at the $p < 0.05$ level are indicate with horizontal black lines (two-tail paired t-test).
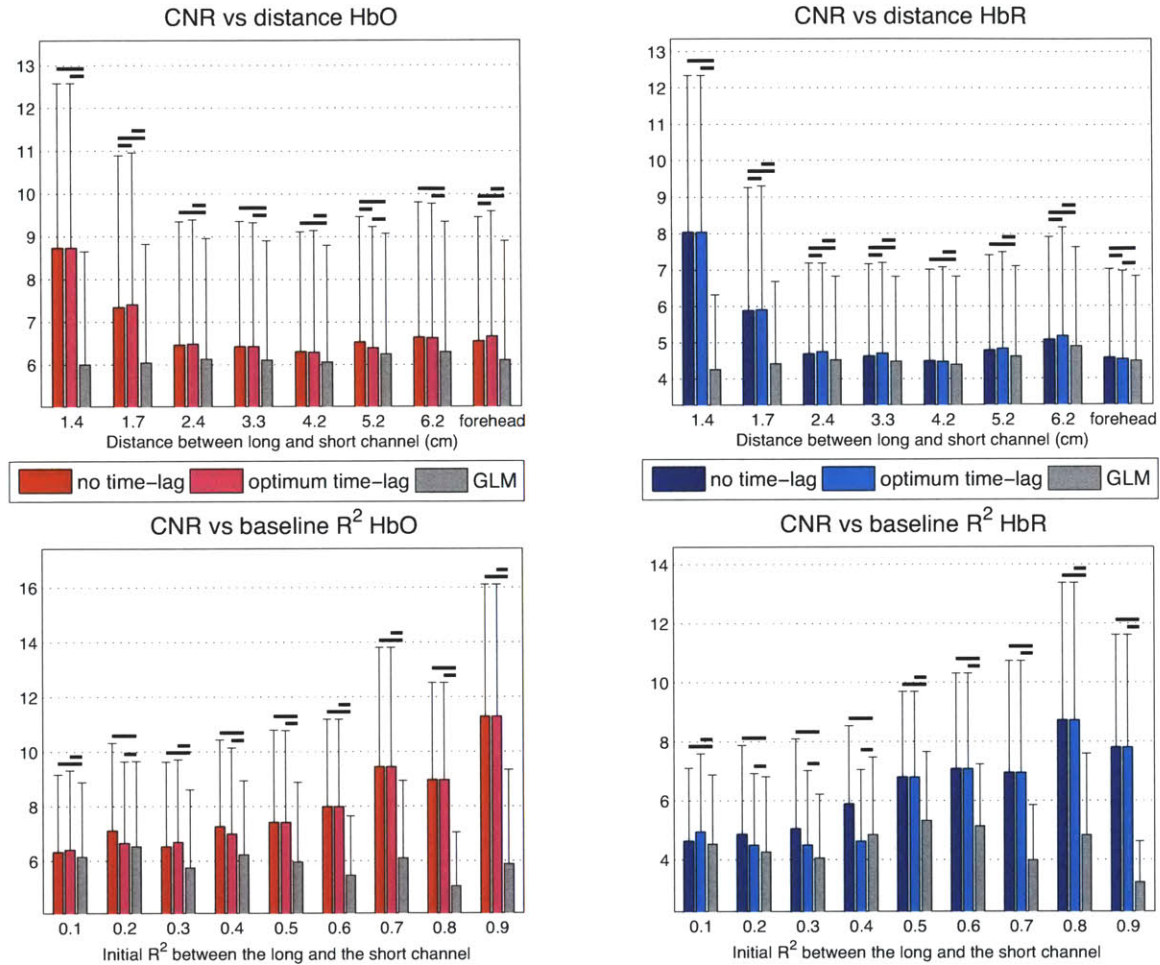
Figure 3-7: Effect of the relative distance on the Contrast-to-noise ratio (CNR) defined in Eq. 3.14. The top panels show the CNR as a function of the distance between the short and the long NIRS channel. The bottom panels show the CNR as a function of the baseline R^2 between the short and the long NIRS channel. The left panels show results for HbO while the right panels show results for HbR. Statistical differences at the $p < 0.05$ level are indicate with horizontal black lines (two-tail paired t-test).

3.2.3 Functional data results

Each run of finger tapping was analysed independently for each subject. The SD pair showing the strongest functional response was selected manually for each subject. The criteria for selecting the responses were a sustained increase in HbO and a sustained decrease in HbR [5] on the HRFs recovered using the Kalman filter with the closest small separation as the regressor. These selected HRFs for the first run are shown in column 4 of Fig. 3-8 for two individual subjects (rows A and B) and for the group average over the 6 subjects (row C). Results from a single run are presented to illustrate the power of our method and the high CNR achieved with only 6 individual finger tapping blocks. Results from the second and the third run were very similar. Columns 1-3 illustrate the corresponding HRFs (same 3 cm channels) recovered using: (1) a block-average with no small separation, (2) the Kalman filter with the small separation located in the forehead as a regressor and (3) the Kalman filter with the short separation located 2.4 cm away as a regressor. Row A illustrates an individual subject for which no clear activation could be observed without using the closest short separation. However, the activation became clear on the same channel using the Kalman filter together with the closest short separation. Row B illustrates another individual subject for which a clear activation was present whether the Kalman filter was used or not. For the group average, the activation was not clear in panels C1-C3 but became very clear using the closest short separation as illustrated in panel C-4.

3.3 Discussion

3.3.1 Systemic interference measured by NIRS is inhomogeneous across the scalp

Systemic interference measured in NIRS has been termed "global" interference previously in the literature [41, 52, 53, 47, 43]. In contradiction, our present results indicate
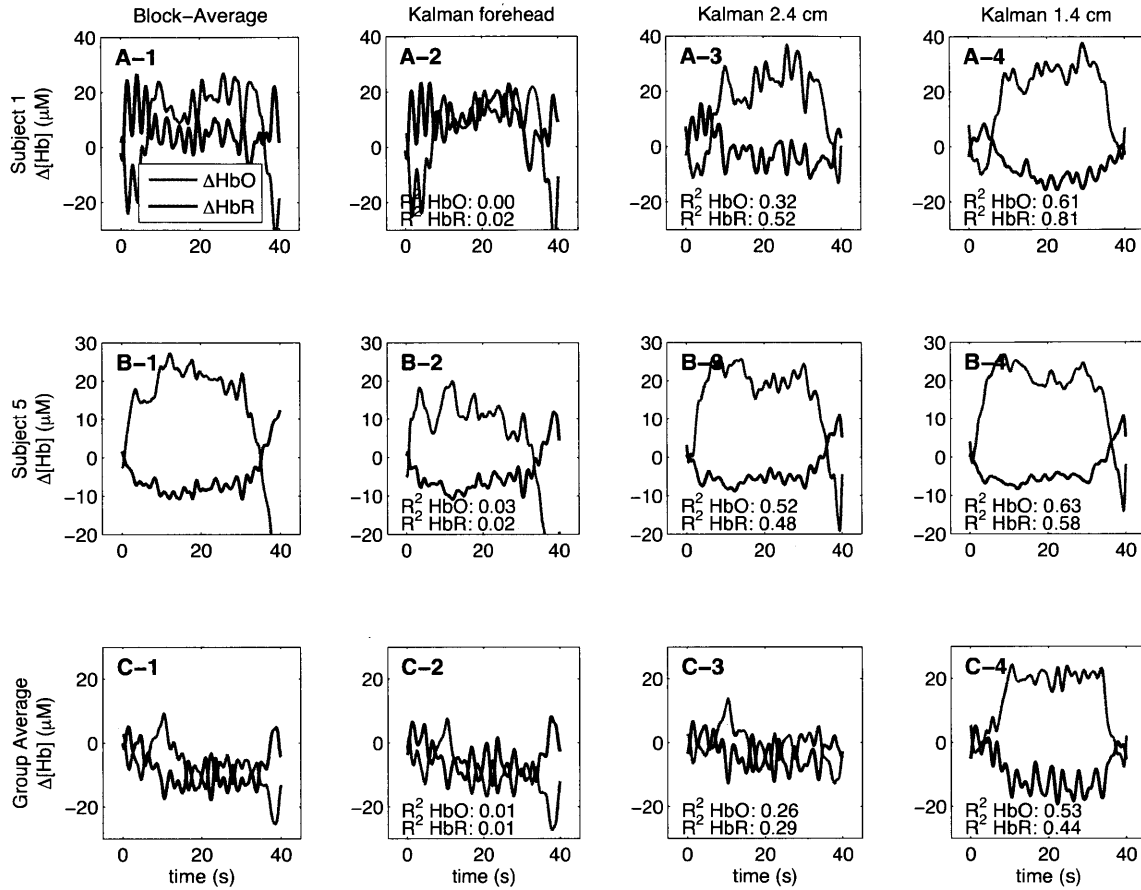
Figure 3-8: Finger tapping results from a single run containing 6 individual blocks. The numbers represent the baseline R^2 correlation between the long and the short NIRS channels used in the analysis. Time courses of the HRFs recovered with (1) a standard block-average (2) the Kalman filter with the forehead short separation (3) the Kalman filter with the short separation located at 2.4 cm and (4) the Kalman filter with the short separation located at 1.4 cm. (A) Representative subject for which no clear response was observed without the Kalman filter. (B) Representative subject for which a clear response was observed even without the Kalman filter. (C) Group average over the 6 subjects.

that systemic interference is actually inhomogeneous across the surface of the scalp, that is, the correlation between systemic interference measured at two different locations decreases with the increasing relative distance between the two measurements. The bottom panels of Fig. 3-4 indicate that the origin of this decorrelation is located in the superficial layers of the head and therefore, is not due to autoregulation mechanisms occurring in the brain tissue [38].

Although introducing a time-lag re-established one third of the correlation between the two short SD measurements, the other two thirds of the R^2 correlation was still lost after introducing time delays. This finding indicates that only part of the correlation decay can be explained by simple transit time effects across different locations on the scalp. The systemic interferences measured in NIRS are oscillatory processes containing three dominant components [33]. These are the cardiac pulsations around 1 Hz, respiratory oscillations around 0.4 Hz and other low frequency oscillations (including Mayer waves [30]) around 0.1 Hz. Analyses similar to the one presented in Fig. 3-4 were performed with the NIRS data bandpass filtered at 0.01-0.2 Hz, 0.2-0.5 Hz and at 0.5-3 Hz (see supplementary figures 3-9, 3-10 and 3-11). These frequency bands correspond to the low frequency, respiratory and cardiac oscillations respectively. These analyses revealed a decay in correlation with increasing relative distances in all these three frequency bands. Although the correlation decayed, it never reached zero even for low frequency oscillations, which is in agreement with recent findings by Tong and Frederick ([45]). Up to 3/4 and 1/2 of the correlation lost in the 0.2-0.5 Hz band and the 0.5-3 Hz band respectiveley could be re-established by introducing a time-lag. However, introducing a time-lag in the 0.01-0.2 Hz frequency band resulted in only negligible improvements in correlation. These findings are in agreement with a recent paper from Tian et al ([44]) indicating that cardiac fluctuations ($\sim$1 Hz) are more global while low frequency oscillations ($\sim$0.1 Hz) are less spatially coherent.

From our results, one can conclude that (1) slow oscillations are inhomogeneous across the surface of the scalp and (2) a significant proportion of the correlation decay in the
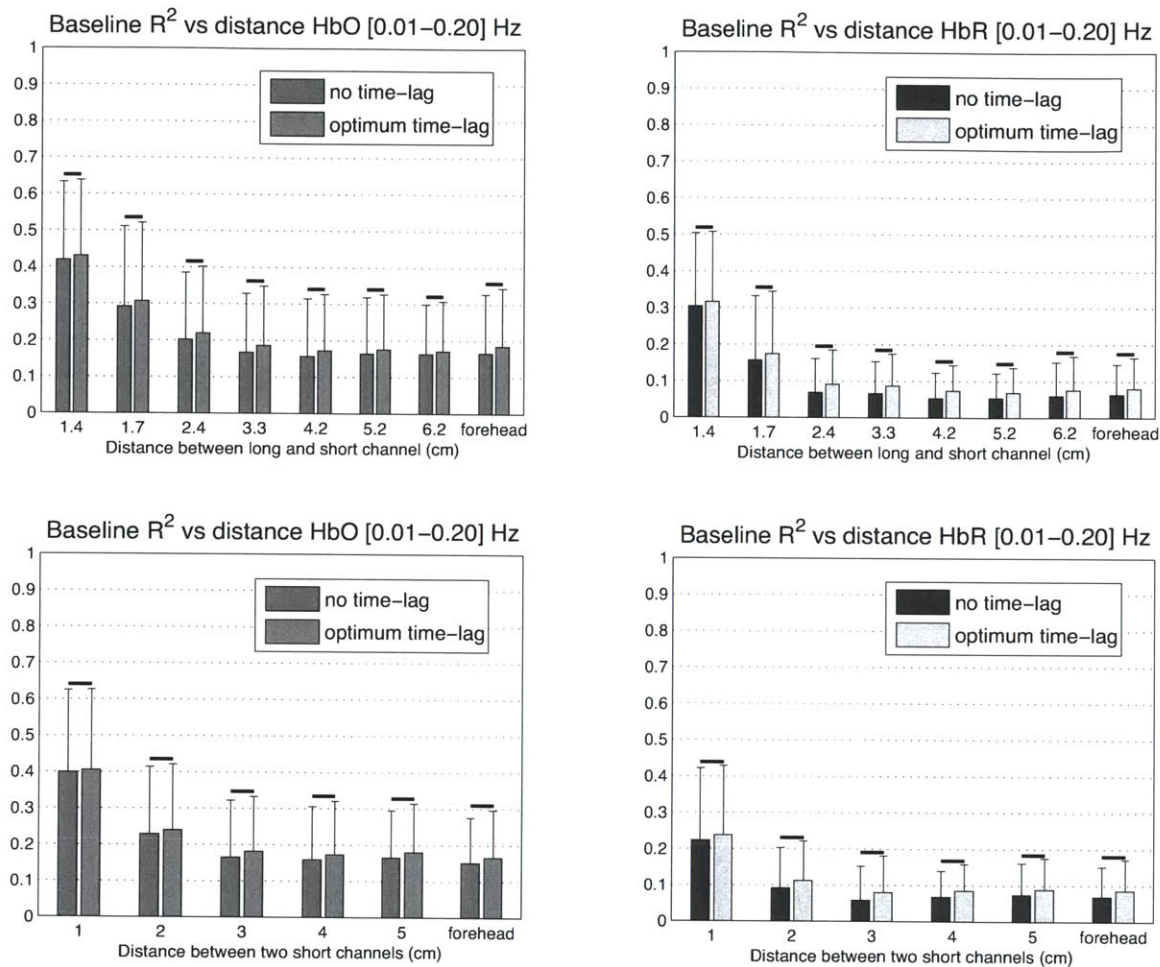
Figure 3-9: Supplementary figure. Effect of the relative distance on the initial baseline correlation between the channels. The baseline data were bandpass filtered between 0.01 and 0.2 Hz (low frequency oscillations) before the R^2 correlation was computed. The values labeled "optimal time-lag" were computed by taking the maximum of the normalized cross-correlation function (Eq. 3.15) while the "no time-lag" values are the standard Pearson R^2 coefficient. Statistical differences at the $p < 0.05$ level are indicate with horizontal black lines (two-tail paired t-test). (Top) Initial baseline R^2 between the long and the short channels as a function of the relative distance between them. (Bottom) Initial baseline R^2 between two short separation channels as a function of the relative distance between them. (left) HbO. (right) HbR.

Figure 3-10: Supplementary figure. Effect of the relative distance on the initial baseline correlation between the channels. The baseline data were bandpass filtered between 0.2 and 0.5 Hz (respiratory oscillations) before the R^2 correlation was computed. The values labeled "optimal time-lag" were computed by taking the maximum of the normalized cross-correlation function (Eq. 3.15) while the "no time-lag" values are the standard Pearson R^2 coefficient. Statistical differences at the $p < 0.05$ level are indicate with horizontal black lines (two-tail paired t-test). (Top) Initial baseline R^2 between the long and the short channels as a function of the relative distance between them. (Bottom) Initial baseline R^2 between two short separation channels as a function of the relative distance between them. (left) HbO. (right) HbR.
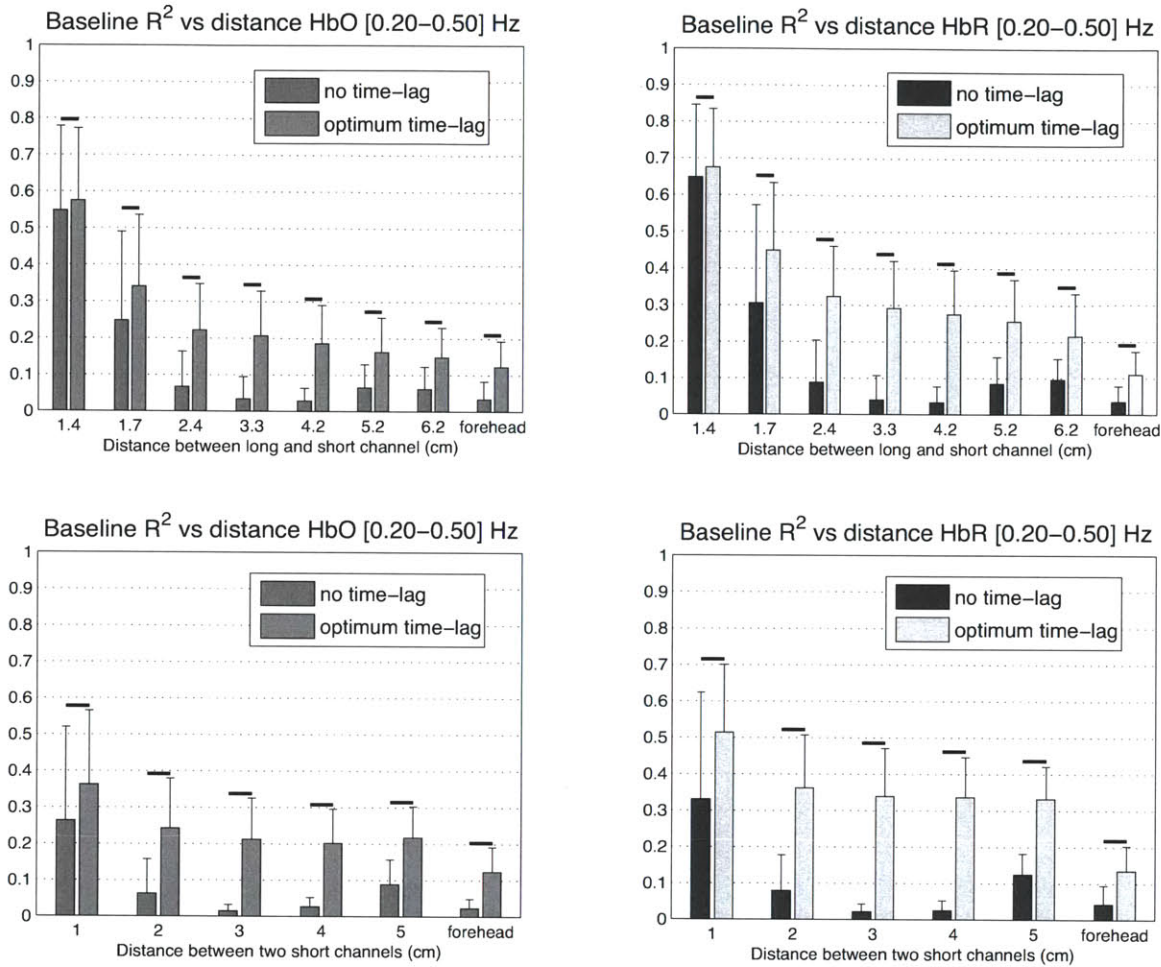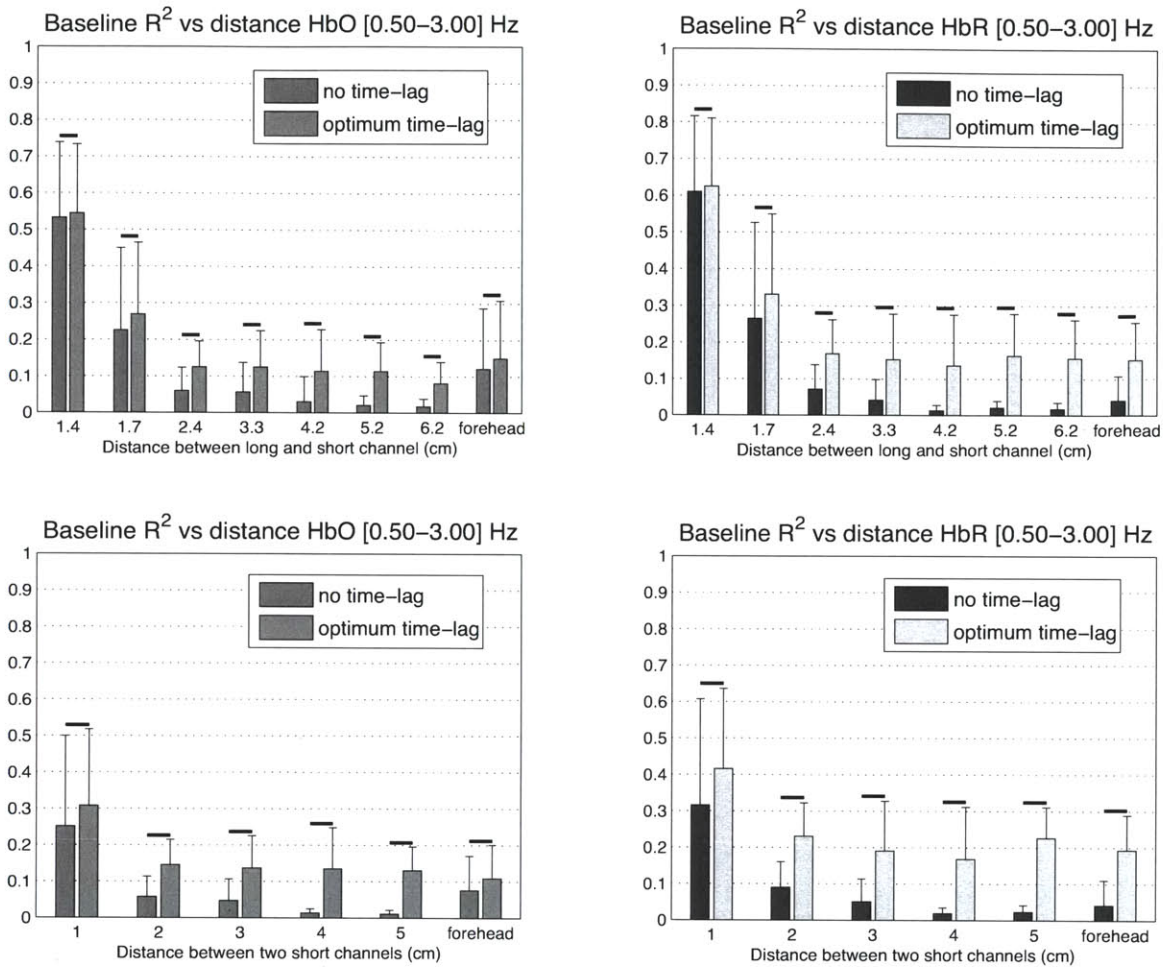
Figure 3-11: Supplementary figure. Effect of the relative distance on the initial baseline correlation between the channels. The baseline data were bandpass filtered between 0.5 and 3 Hz (cardiac oscillations) before the R^2 correlation was computed. The values labeled "optimal time-lag" were computed by taking the maximum of the normalized cross-correlation function (Eq. 3.15) while the "no time-lag" values are the standard Pearson R^2 coefficient. Statistical differences at the $p < 0.05$ level are indicate with horizontal black lines (two-tail paired t-test). (Top) Initial baseline R^2 between the long and the short channels as a function of the relative distance between them. (Bottom) Initial baseline R^2 between two short separation channels as a function of the relative distance between them. (left) HbO. (right) HbR.

63

higher frequency bands (cardiac and respiration) is attributed to transit time effects across different spatial regions. These phase mismatches of the cardiac and respiratory pulsation over different locations arise potentially from spatial heterogeneity of the vasculature such as blood vessel length, orientation, size, depth and dilation [52, 51]. However, 1/4 and 1/2 of the correlation lost in the respiration and cardiac frequency band respectively could not be re-established by introducing a time-lag and future studies will be required to investigate the origin of this correlation decay.

3.3.2   Impact on the short separation method

This decrease in correlation with increasing relative distance has an important impact on the performance of the short separation method. The bottom panels of Figs. 3-5, 3-6 and 3-7 illustrate that all three metrics used (R^2, MSE and CNR) varied linearly with the baseline correlation, whether a time-lag was used or not. Since the baseline correlation decreased with the relative distance as shown in Fig. 3-4, we expected the performance of the short separation method assessed with these three metrics to decrease with the relative distance. This expectation was confirmed by our simulations and are shown in the top panels of Figs. 3-5, 3-6 and 3-7. For relative distances larger than 2 cm, only mild improvements were obtained using our short separation approach compared to the standard GLM method. However, this improvement was still significant ($p < 0.05$, two-tailed paired t-test). No decrease in performance was observed using our Kalman filter with any of the available short separation. This is consistent with our previous findings [11] that the Kalman filter improves or doesn't change recovery of the hemodynamic response. At worst, the recovered response will be the same as the one recovered with a standard GLM with no small separation used. To obtain larger improvements that are useful in practice, the short separation measurement must be located no more than 1.5 cm from the 3 cm SD pair from which the HRF is to be recovered.

For large NIRS probes containing several long SD measurements spread over several

centimeters, our results indicate that multiple short separation channels are required in order to combine each long SD measurement with a short separation within a 1.5 cm radius. In this case, our simulations indicate that the improvement in CNR using the short separation method is of the order of 50 % for HbO and 100 % for HbR, as shown in the top panels of Fig. 3-7. As in our previous paper [11], we observed an improvement for both HbO and HbR, in contradiction with Zhang et al [51] where no improvement was observed for HbR using an adaptive filter method. In the simulations of our previous paper [11], we also observed a decrease in performance for HbR using an adaptive filter. As we showed, our Kalman filter approach overcomes this pitfall by regressing the short separation measurement and simultaneously estimating the hemodynamic response.

The necessity of using several short separations was also confirmed by our finger tapping experiment. Using the short separation located at 2.4 cm from the 3 cm measurement, the HRF obtained by averaging across the 6 subjects did not show a clear activation pattern (sustained increase in HbO and sustained decrease in HbR) as shown in Fig. 3-8 C-3. On the other hand, the activation became very clear in Fig. 3-8 C-4 using the short separation located 1.4 cm away. As shown in Fig. 3-8, the baseline correlations between the 1 cm and the 3 cm channels were around 0.3 for the short separation located 2.4 cm away and around 0.5 for the short separation located 1.4 cm away. This re-emphasizes the fact that the initial baseline correlation between the 1 cm and the 3 cm channel is an important factor in determining the performance of the Kalman filter algorithm. In practice, this baseline correlation can be computed to predict the impact of using short optode separations. In our previous paper [11], we showed that the presence of a hemodynamic response in the 3 cm channel does not impact the baseline initial correlation between the 1 cm and the 3 cm channel. This occurs because the contribution of systemic interference in NIRS largely dominates the contribution of the hemodynamic response. This was confirmed here with our real functional data.

3.3.3 Future studies

In this work, a single small separation channel was used for every long SD channel. This was necessary since two small separations could not fit between the source and the detector of the longer SD channel on our probe. In future work, it would be interesting to design a small separation channel integrated in every source and detector optode of the 3 cm measurements. Doing so would allow to use two small separations for each long SD channel. This would maximize the overlap between the pathlength of the small separation channels and the longer SD channel, and might result in a further improvement of the small separation method.

3.4   Summary

In this study, we have determined that the position of the short SD separation relative to the long SD separation impacts the performance of the short separation regression method to improve the recovery of the hemodynamic response in NIRS. We showed that the relative distance between the channel of interest and the regressor must be less than 1.5 cm to have a meaningful impact on the recovery of the hemodynamic response. In this case, improvements in CNR were of the order of 50 % for HbO and 100 % for HbR compared to the standard GLM approach. When a short separation located farther than 2 cm was used as a regressor, only minor improvements were obtained compared to the standard GLM method, which are of little practical use. This decrease in performance for longer relative distances results from a decrease in the baseline correlation between the channel of interest and the regressor. Our results indicate that this correlation decay is due to spatially inhomogeneous hemodynamics in the superficial layers of the head.

Chapter 4

Conclusion

The state-space model developed in this work allowed us to improve the recovery of the hemodynamic response with NIRS, by accounting for the dynamic physiological fluctuations present in the signal, as well as by taking advantage of the simultaneous estimation and regression. NIRS is mostly used in a setting with low contrast-to-noise ratio, such as newborn imaging and epilepsy monitoring, due to the difficulty of repeating the measurement multiple times for averaging. As such, the improvement in contrast-to-noise ratio achieved by our method will have a tremendous impact on the NIRS community. Moreover, we were able to test in details the accuracy of the method, identify its weakness and propose solutions to compensate for this weakness by introducing multiple short separation optodes. The method developed in this work is easily implementable and can be used in a vast majority of NIRS experiments.

Bibliography

[1] A. F. Abdelnour and T. J. Huppert. Real-time imaging of humain brain function by near-infrared spectroscopy using an adaptive general linear model. *NeuroImage*, 46:133–143, 2009.

[2] D.A. Boas, A. M. Dale, and M. A Franceschini. Diffuse optical imaging of brain activation: Approaches to optimizing image sensitivity, resolution and accuracy. *NeuroImage*, 23:S275–S288, 2004.

[3] D. H. Brainard. The psychophysics toolbox. *Spatial Vision*, 10:433–436, 1997.

[4] M. Cope and D. T. Deply. System for long-term measurement of cerebral blood flow and tissue oxygenation on newborn infants by infrared transillumination. *Med. Biol. Eng. Comput.*, 26:289–294, 1998.

[5] X. Cui, S. Bray, and A. L. Reiss. Functional near infrared spectroscopy (NIRS) signal improvement based on negative correlation between oxygenated and de-oxygenated hemoglobin dynamics. *NeuroImages*, 49:3039–3046, 2010.

[6] D. T. Deply, M. Cope, P. van der Zee, S. Arridge, S. Wray, and J. Wyatt. Estimation of optical pathlength through tissue from direct time of flight measurement. *Phys. Med. Biol.*, 33:1433–1442, 1988.

[7] S. Diamond, T. J. Huppert, V. Kolehmainen, M. A. Franceschini, J. P. Kaipo, S. R. Arridge, and D. A. Boas. Dynamic physiological modeling for functional diffuse optical tomography. *NeuroImage*, 30:88–101, 2006.

[8] S. G. Diamond, K. L. Perdue, and D. A. Boas. A cerebrovascular response model for functional neuroimaging including dynamic cerebral autoregulation. *Math. Biosci.*, 220(2):102–117, 2009.

[9] M.A. Franceschini, S. Fantini, J.H. Thompson, J.P. Culver, and D.A. Boas. Hemodynamic evoked response of the sensorimotor cortex measured noninvasively with near-infrared optical imaging. *Psychophysiology*, 40(4):548–560, 2003.

[10] M.A. Franceschini, D. K. Joseph, T. J. Huppert, S. G. Diamond, and D.A. Boas. Diffuse optical imaging of the whole head. *J. Biomed. Opt.*, 11(5):054007, 2006.

[11] L. Gagnon, K. Perdue, D. N. Greve, D. Goldenholz, G. Kaskhedikar, and D. A. Boas. Improved recovery of the hemodynamic response in diffuse optical imaging using short optode separations and state-space modeling. *NeuroImage*, 56(3):1362–1371, 2011.

[12] A. Gelb. *Applied Optimal Estimation.* MIT Press, 1974.

[13] A.P. Gibson, J.C. Hebden, and S.R. Arridge. Recent advances in diffuse optical imaging. *Phys. Med. Biol.*, 50:R1–R43, 2005.

[14] G. H. Glover. Deconvolution of impulse response in event-related bold fmri. *NeuroImage*, 9(4):416–429, 1999.

[15] G. Gratton and P. M. Corballis. Removing the heart from the brain: compensation for the pulse artifact in the photon migration signal. *Psychophysiology*, 32(3):292–299, 1995.

[16] N. M. Gregg, B. R. White, B. W. Zeff, A. J. Berger, and J. P. Culver. Brain specificity of diffuse optical imaging: improvements from superficial signal regression and tomography. *Font. in Neuroenergetics*, 2(14):1–8, 2010.

[17] Simon Haykin. *Adaptive Filter Theory.* Prentice-Hall, Upper Saddle River, NJ, 2001.

[18] Simon Haykin. *Kalman filtering and neural Networks*. John Wiley & Sons, New York, 2001.

[19] E. M. C. Hillman. Optical brain imaging in vivo: techniques and applications from animal to man. *J. Biomed. Opt.*, 12(5):051402, 2007.

[20] Y. Hoshi. Functional near-infrared spectroscopy: current status and future prospects. *J. Biomed. Opt.*, 12(6):062106, 2007.

[21] X.-S. Hu, K.-S. Hong, S. S. Ge, and M.-Y. Jeong. Kalman estimator- and general linear model-based on-line brain activation mapping by near-infrared spectroscopy. *BioMedical Engineering OnLine*, 9(82), 2010.

[22] T. J. Huppert. *Hemodynamic-Based Inference of Cerebral Oxygen Metabolism*. PhD thesis, Harvard University, 2007.

[23] T. J. Huppert, M. S. Allen, S. G. Diamond, and D. A. Boas. Estimating cerebral oxygen metabolism from fmri with a dynamic multicompartment windkessel model. *Hum. Brain Mapp.*, 30(5):1548–1567, 2009.

[24] T. J. Huppert, S. G. Diamond, and D. A. Boas. Direct estimation of evoked hemoglobin changes by multimodality fusion imaging. *J. Biomed. Opt.*, 13(5):054031, 2008.

[25] T.J. Huppert, M. S. Allen, H. Benay, P. B. Jones, and D.A. Boas. A multicompartment vascular model for inferring baseline and functional changes in cerebral oxygen metabolism and arterial dilation. *J. Cereb. Blood Flow Metab.*, 27:1262–1279, 2007.

[26] T.J. Huppert, R.D. Hoge, A. M. Dale, M.A. Franceschini, and D.A. Boas. Quantitative spatial comparison of diffuse optical imaging with blood oxygen level-dependent and arterial spin labeling-based functional magnetic resonance imaging. *J. Biomed. Opt.*, 11(6):064018, 2006.

[27] T.J. Huppert, R.D. Hoge, S.G. Diamond, M.A. Franceschini, and D.A. Boas. A temporal comparison of BOLD, ASL, and NIRS hemodynamic responses to motor stimuli in adult humans. *NeuroImage*, 29:368–382, 2006.

[28] K. E. Jang, S. Tak, J. Jung, J. Jang, Y. Jeong, and J. C. Ye. Wavelet minimum description length detrending for near-infrared spectroscopy. *J. Biomed. Opt.*, 14(3):034004, 2009.

[29] G. Jasdzewski, G. Strangman, J. Wagner, K. K. Kwong, R. A. Poldorack, and D. A. Boas. Differences in the hemodynamic response to event-related motor and visual paradigms as measured by near- infrared spectroscopy. *NeuroImage*, 20(1):479–488, 2003.

[30] C. Julien. The enigma of Mayer waves: facts and models. *Cardiovascular Research*, 70:12–21, 2007.

[31] R. E. Kalman. A new approach to linear filtering and prediction problems. *Journal of Basic Engineering*, 82(Series D):35–45, 1960.

[32] V. Kolehmainen, S. Prince, S. R. Arridge, and J. P Kaipo. State- estimation approach to the nonstationary optical tomography problem. *J. Opt. Soc. Am. A*, 20(5):876–889, 2003.

[33] J-M. Lina, M. Dehaes, C. Matteau-Pelletier, and F. Lesage. Complex wavelets applied to diffuse optical spectroscopy for brain activity detection. *Optics Express*, 16(2):1029–1050, 2008.

[34] J-M. Lina, C. Matteau-Pelletier, M. Dehaes, M. Desjardins, and F. Lesage. Wavelet-based estimation of the hemodynamic responses in diffuse optical imaging. *Med. Imag. Anal.*, 14:606–616, 2010.

[35] C. Matteau-Pelletier, M. Dehaes, F. Lesage, and J-M. Lina. 1/f noise in diffuse optical imaging and wavelet-based response estimation. *IEEE Trans. Med. Imag.*, 28:415–422, 2009.

[36] H. Obrig, M. Neufang, R. Wenzel, M. Kohl, J. Steinbrink, K. Einhaupl, and A. Villringer. Spontaneous low frequency oscillations of cerebral hemodynamics and metabolism in human adults. *NeuroImage*, 12(6):623–639, 2000.

[37] Y. Obrig and A. Villringer. Beyond the visible: imaging the human brain with light. *J. Cereb. Blood Flow Metab.*, 23:1–18, 2003.

[38] S. Payne, J. Selb, and D. A. Boas. Effects of autoregulation and CO2 reactivity on cerebral oxygen transport. *Ann. Biomed. Eng.*, 37(11):2288–2298, 2009.

[39] S. Prince, V. Kolehmainen, J. P. Kaipo, M. A. Franceschini, D. A Boas, and S. R. Arridge. Time-series estimation of biological factors in optical diffusion tomography. *Phys. Med. Biol.*, 48:1491–1504, 2003.

[40] H. E. Rauch, , F. Tung, and C. T. Striebel. Maximum likelihood estimates of linear dynamic systems. *AIAA Journal*, 3(8):1445–1450, 1965.

[41] Rolf B. Saager and Andrew J. Berger. Direct characterization and removal of interfering absorption trends in two-layer turbid media. *J. Opt. Soc. Am. A*, 22(9):1874–1882, 2005.

[42] Rolf B. Saager and Andrew J. Berger. Measurement of layer-like hemodynamic trends in scalp and cortex: implications for physiological baseline suppression in functional near-infrared spectroscopy. *J. Biomed. Opt.*, 13(3):034017, 2008.

[43] Rolf B. Saager, Nicole L. Telleri, and Andrew J. Berger. Two-detector corrected near infrared spectroscopy (C-NIRS) detects hemodynamic activation responses more robustly than single-detector NIRS. *NeuroImage*, 55(4):1679–1685, 2011.

[44] F. Tian, H. Niu, B. Khan, G. Alexandrakis, K. Behbehani, and H. Liu. Enhanced functional brain imaging by using adaptive filtering and a depth compensation algorithm in Diffuse Optical Tomography. *IEEE Trans. Medical Imaing*, 30(6):1239–1251, 2011.

[45] Yunjie Tong and Blaise deB Frederick. Time lag dependent multimodal processing of concurrent fMRI and near-infrared spectroscopy (NIRS) data suggests a global circulatory origin for low-frequency oscillation signals in human brain. *NeuroImage*, 53(2):553–564, 2010.

[46] V. Tonorov, M. Franceschini, M. Filiaci, S. Fantini, M. Wolf, A. Michalos, and E. Gratton. Near-infrared study of fluctuations in cerebral hemodynamics during rest and motor stimulation: temporal analysis and spatial mapping. *Med. Phys.*, 27(4):801–815, 2000.

[47] S. Umeyama and T. Yamada. Monte carlo study of global interference cancellation by multidistance measurement of near-infrared spectroscopy. *J. Biomed. Opt.*, 14(6):064025, 2009.

[48] A. Villringer, C. Hock, L. Schleinkofer, and U. Dirnagl. Near infrared spectroscopy (NIRS): A new tool to study hemodynamic changes during activation of brain function in human adults. *Neurosci. Lett.*, 154:101–104, 1993.

[49] T. Yamada, S. Umeyama, and K. Matsuda. Multidistance probe arrangement to eliminate artifacts in functional near-infrared spectroscopy. *J. Biomed. Opt.*, 16(4):06434, 2009.

[50] Q. Zhang, D. H. Brooks, M. A. Franceschini, and D. A. Boas. Eigenvector-based spatial filtering for reduction of physiological interference in diffuse optical imaging. *J. Biomed. Opt.*, 10(1):011014, 2005.

[51] Q. Zhang, G. Strangman, and G. Ganis. Adaptive filtering to reduce global interference in non-invasive nirs measures of brain activation: How well and when does it work? *NeuroImage*, 45:788–794, 2009.

[52] Quan Zhang, Emery N. Brown, and Gary E. Strangman. Adaptative filtering for global interference cancellation and real-time recovery of evoked brain activity: a Monte Carlo simulation study. *J. of Biomed. Opt.*, 12(4):044014, 2007.

[53] Quan Zhang, Emery N. Brown, and Gary E. Strangman. Adaptative filtering to reduce global interference in evoked brain activity detection: a human subject case study. *J. of Biomed. Opt.*, 12(6):064009, 2007.